



HAL
open science

Non-linear modulation of site response: Sensitivity to various surface ground-motion intensity measures and site-condition proxies using a neural network approach

Boumédiène Derras, Pierre-Yves Bard, Julie Régnier, Héroïse Cadet

► To cite this version:

Boumédiène Derras, Pierre-Yves Bard, Julie Régnier, Héroïse Cadet. Non-linear modulation of site response: Sensitivity to various surface ground-motion intensity measures and site-condition proxies using a neural network approach. *Engineering Geology*, 2020, 269, pp.105500. 10.1016/j.enggeo.2020.105500 . hal-03035534

HAL Id: hal-03035534

<https://hal.science/hal-03035534>

Submitted on 20 May 2022

HAL is a multi-disciplinary open access archive for the deposit and dissemination of scientific research documents, whether they are published or not. The documents may come from teaching and research institutions in France or abroad, or from public or private research centers.

L'archive ouverte pluridisciplinaire **HAL**, est destinée au dépôt et à la diffusion de documents scientifiques de niveau recherche, publiés ou non, émanant des établissements d'enseignement et de recherche français ou étrangers, des laboratoires publics ou privés.



Distributed under a Creative Commons Attribution - NonCommercial 4.0 International License

1 **NON-LINEAR MODULATION OF SITE RESPONSE:**
2 **SENSITIVITY TO VARIOUS SURFACE GROUND-MOTION INTENSITY**
3 **MEASURES AND SITE- CONDITION PROXIES USING A NEURAL**
4 **NETWORK APPROACH**

5
6 **Boumediène Derras** ⁽¹⁾, **Pierre-Yves Bard** ⁽²⁾, **Julie Régnier** ⁽³⁾, and
7 **Héloïse Cadet** ⁽⁴⁾

8
9 ⁽¹⁾ RISAM Laboratory, University of Tlemcen, BP 230, 13048, Chetouane, Tlemcen.
10 Department of Civil Engineering and Hydraulics, University of Saïda, Algeria.
11 boumediene.derras@univ-tlemcen.dz.

12 ⁽²⁾ Univ. Grenoble Alpes, Univ. Savoie Mont-Blanc, CNRS, IRD, IFSTTAR, ISTerre, Bâtiment
13 OSUG C, CS 40700, 38058 GRENOBLE Cedex 9, France; pierre-yves.bard@univ-grenoble-
14 alpes.fr

15 ⁽³⁾ CEREMA, DTer Méditerranée, 56 Boulevard de Stalingrad, 06300 Nice, France;
16 Julie.regnier@cerema.fr

17 ⁽⁴⁾ ADRGT, 2 Rue de La Condamine, ZI de Mayencin, 38610 Gières, France. h.cadet@adrgt.org

18
19 **ABSTRACT**

20 The impact of non-linear soil behavior on site response may be described by the non-
21 linear to linear site response ratio RSR_{NL} introduced in Régnier et al. (2013). This
22 ratio most often exhibits a typical shape with an amplitude above one below a site-
23 specific frequency f_{NL} , and an amplitude below one beyond f_{NL} . This paper presents
24 an investigation of the correlation between this RSR_{NL} ratio and various parameters

25 used to characterize the site (Site Condition Proxies: SCPs) and the seismic loading
26 level (Ground Motion Intensity Measures: GMIMs).

27 The data used in this analysis come from sites of the Japanese Kiban–Kyoshin (KiK-
28 net) network, for which the nonlinear to linear site-response ratio (RSR_{NL}) is obtained
29 by comparing the surface/down-hole Fourier spectral ratio for strong events and for
30 weak events. The five SCPs are V_{S30} , the minimum velocity of the soil profile (V_{Smin}),
31 an index of the velocity gradient over the top 30 m (B_{30}), the fundamental frequency
32 f_{0HV} , as measured from the H/V earthquake ratio, and the corresponding amplitude
33 A_{0HV} . The seven GMIMs are PGA, PGV, PGV/V_{S30} (peak strain proxy), I_A (Arias
34 Intensity), CAV (Cumulative Absolute Velocity), a_{rms} (Root Mean Square
35 Acceleration) and Trifunac-Brady Duration (D_T). The original data set consists of a
36 total of 2927 RSR_{NL} derived from KiK-net recordings at 132 sites. To assign an equal
37 weight to each site, and to avoid any bias linked to sites with many recordings, for
38 each GMIM, this original data set is grouped in 15 different intervals corresponding to
39 fixed fractiles of the statistical distribution of the considered GMIM (every 10% from
40 F10 to F50, and every 5% from F55 to F100). In each group, the average RSR_{NL-GM}
41 for each site is computed. For each of these seven advanced data sets, a neural
42 network approach is used to predict the behavior of RSR_{NL-GM} as a function of the
43 corresponding GMIM, and one or two SCPs. The performance of each model is
44 quantified through the average variance reduction coefficient $\mu(Rc)$ in a fixed
45 frequency range. This sensitivity study is performed in the normalized frequency
46 (f/f_{NL}) domain to identify the best combinations (GMIM, SCPs) providing the largest
47 variance reduction, and then in the absolute frequency domain for the final optimal
48 combination. The optimal combinations [GMIM, two-SCPs] are triplets [PGV / V_{S30} ,
49 $V_{S30}-f_{0HV}$; $\mu(Rc) = 18.6\%$], [PGV / V_{S30} , $V_{S30}-A_{0HV}$; $\mu(Rc) = 18.16\%$], [PGV , $V_{S30}-f_{0HV}$;

50 $\mu(R_c) = 17.3\%$] and [PGA, $B_{30-A_{0HV}}$; $\mu(R_c) = 17.2\%$]. The final absolute frequency
51 model with the best triplet makes it possible to predict the non-linear response of a
52 given site knowing its linear, weak-motion response, and two site proxy parameters,
53 for wide ranges of the considered ground motion parameters.
54 Keywords: Non-linear site response, site-specific frequency, Site Condition Proxies,
55 Ground Motion Intensity Measures, neural networks.

56 **1 INTRODUCTION**

57 Although the Non-Linear (so-called NL) behavior of soft soils under large seismic
58 shaking has been recognized since many decades, accounting for NL site response
59 in hazard assessment studies is still associated with large uncertainties. The various
60 benchmarking exercises of NL simulation codes over the last 2 decades, reported in
61 Kwok et al., (2008), Stewart (2008), Stewart and Kwok (2008, 2009), and Régnier et
62 al., (2016a, 2018), have repeatedly shown that the prediction of site-specific NL
63 response may vary significantly even amongst teams with very good expertise in NL
64 simulation, due to various types of uncertainties linked either to the simulation (code
65 and numerical method, constitutive model, user) or to the definition and
66 measurement of soil parameters, together with intrinsic assumptions of the model
67 (1D site impinged by vertically propagating S waves, with or without pore-water
68 pressure effects). All these uncertainties lead to a simulation-to-simulation variability
69 reaching 0.25 (\log_{10} scale), and prediction to observations differences up to 0.25 to
70 0.35 (\log_{10} scale) especially around the site fundamental frequency.
71 On another hand, more generic seismic hazard estimates based on GMPEs face
72 difficulties in accounting for NL site response: amongst the GMPEs that include NL

73 site terms, only very few are based exclusively on recorded data (Sandikkaya et al.,
74 2013, Derras et al., 2016, 2017), while most of them constrain the NL site term with
75 complementary 1D simulations (described in Walling et al., 2008 for NGA models,
76 and Kamai et al., (2014) and Seyhan and Stewart 2014 for NGA West 2 models).
77 The resulting site term models are thus also depending a lot on the simulation
78 assumptions and are impacted by all the corresponding uncertainties.

79 The global objective of the present study is to propose an alternative, purely
80 empirical approach, that could be used for both site-specific and generic studies. It
81 focuses only on one peculiar aspect of NL site response, i.e., the changes in site
82 response due to the NL behavior of soils. Such modifications have already been
83 reported many times since the early nineties on individual data sets (e.g., SMART1
84 array in Taiwan, a few pre KiK-net borehole recordings in Japan, some rock/soil
85 station pairs in California, and the large set of mainshock/aftershock recordings in the
86 Los Angeles basin from the Northridge sequence, see Field et al., 1997). The
87 number of such recordings exhibiting NL response has increased a lot in the last two
88 decades, especially with the KiK-net data. This led Régnier et al., (2013) to propose
89 the concept of "non-linear to linear site response ratio" (RSR_{NL}) comparing the
90 surface/downhole Fourier spectral ratio for strong events and for weak events, and
91 Régnier et al., (2016a) to present a statistic of such ratios for different groups of sites
92 and different PGA thresholds. This RSR_{NL} modulation function exhibits a typical
93 shape with an amplitude above one at low frequency (due to the shift of resonant
94 frequency associated to shear modulus reduction), and below one at high frequency
95 (associated to increased damping), with a transition frequency denoted f_{NL} , which is
96 site-specific, and always larger than or equal to the site fundamental frequency f_0 .

97 The main goal of the present study is to go one step further, and to propose a model

98 describing the continuous dependence of this RSR_{NL} as a function of the site
99 parameters (Site Condition Proxies: SCPs) and the seismic loading level (Ground
100 Motion Intensity Measures: GMIMs). Such empirical modulation functions could then
101 be used as an alternative to numerical simulation to modify either the linear site
102 transfer functions (observed or simulated) for site-specific hazard estimates, or the
103 linear site terms in GMPEs for generic hazard estimates.

104 The derivation of these empirical modulation functions is described in four main
105 sections. The first one describes the construction of the RSR_{NL} data sets on the basis
106 of a subset of KiK-net recordings for sites having at least one strong recording
107 (surface $PGA \geq 0.1$ g), and two weak motion recordings (PGA between 0.1 and 25
108 cm/s^2), grouped within increasing loading level bins considering various ground
109 motion intensity measures. It also provides an overview of the corresponding
110 statistical distribution of several site parameters to test their ability to predict the NL
111 site response. The second section presents the neural network approach adopted for
112 investigating the dependency of RSR_{NL} on the loading level and various
113 combinations of site proxies, together with the variance reduction metrics adopted to
114 compare the performance of various models. The third and fourth sections present
115 the results of the neural network models, first in a normalized frequency domain
116 [$RSR_{NL}(f/f_{NL})$] to better identify the most relevant SCPs and GMIMs that provide best
117 predictions (those associated with the largest variance reduction), and then in the
118 absolute frequency domain [$RSR_{NL}(f)$] in order to avoid the need to establish a
119 parallel model predicting f_{NL} for each site.

120 **2 FROM RAW DATA TO ADVANCED DATA SETS**

121 The present study requires two kinds of data to build prediction models: a set of
122 linear to non-linear empirical modulation observations, and a set of explanatory
123 variables related to site conditions and loading levels. Presently, the only network
124 offering that combination of high-quality data for a large number of sites with
125 homogeneous site metadata and with a large number of strong enough recordings, is
126 the Japanese Kiban–Kyoshin Network (KiK-net). The KiK-net network consists of 688
127 stations with surface and downhole accelerometers (Fujiwara et al., 2004). Most of
128 the borehole seismic stations are located between 100 and 200 m depth.

129 We start below with the presentation of the model parameters (site condition proxies
130 and loading level parameters), and then describe the building of the empirical non-
131 linear modulation ratios.

132 **2.1 Model parameters**

133 From this KiK-net database and for the purpose of this analysis we extracted two
134 kinds of parameters which may be considered as useful proxies to characterize the
135 non-linear site response: Ground Motion Intensity Measures (GMIMs) related to the
136 loading level from the earthquake recordings, and Site-Condition Proxies (SCPs)
137 related to the site (elastic) properties. Both types of proxies are detailed below.

138 ***2.1.1 Ground-motion intensity measures (GMIMs)***

139 We considered seven different intensity measures to characterize the level of
140 loading: PGA (Peak Ground Acceleration), PGV (Peak Ground Velocity), PGV/V_{S30}
141 (proxy for peak strain, CAV (Cumulative absolute Velocity), IA (arias Intensity), Arms
142 (Root Mean Square Acceleration), and D_T (5%-95% Trifunac-Brady Duration,

143 Trifunac and Brady 1975). The first two are very well known and involve only peak
144 values reached only once during the whole duration of the shaking. The third one is
145 more and more used in the geotechnical earthquake engineering community (see
146 Idriss, 2011), because of its simple and robust physical basis: for a non-dispersive
147 waveform $f(t-x/c)$ propagating along direction x with a propagation speed c , the strain
148 (i.e., the spatial derivative of the motion), is equal to the particle velocity (time
149 derivative of the signal) divided by the propagation speed c . Despite the actual of
150 complexity of seismic wave fields (consisting of multiple waves propagating in
151 various direction with different velocities), the proxy PGV/V_{S30} has been shown to
152 provide a reasonable estimate of peak strains, at least for vertically propagation
153 shear waves (see Chandra et al., 2016; Guéguen et al., 2019), and as long as the
154 soil is not driven too far in the non-linear domain leading to major changes in the
155 propagation velocity and frequency content. The last four GMIMs are derived directly
156 from time domain integration of the acceleration time histories: CAV is obtained by
157 integrating the absolute value of the acceleration time series over the strong motion
158 phase, while IA, Arms and D_T are derived from the "Husid" plot describing the time
159 dependence of the integral of the square of the acceleration time series (Trifunac &
160 Brady, 1975). CAV, IA and Arms combine information on both amplitude and
161 duration, while DT only keeps the duration information.

162

163 **2.1.2 Site-condition proxies (SCPs)**

164 We considered five parameters partially describing the site conditions : V_{S30} (the
165 widely used travel-time average shear wave velocity over the first 30 m of soil), V_{smin}
166 (the minimum shear wave velocity of the soil profile, generally located at the very

167 surface but not always in case of velocity inversion at some depth), B_{30} describing a
168 power-law dependence of V_s with depth, over the top 30m, as defined in Régnier et
169 al. (2013) and Régnier et al (2014), f_{0HV} that is the fundamental resonance frequency
170 picked on the Horizontal to vertical Fourier spectral ratio of surface earthquake
171 recordings, and A_{0HV} the corresponding amplitude.

172 These five proxies provide different kinds of information on the underground
173 structure. The V_{S30} and V_{Smin} parameters provide both an indication on the soil
174 softness at shallow depth. For thin deposits (i.e., with a total thickness less than 30
175 m), the V_{S30} value may be strongly contaminated by the underlying bedrock velocity,
176 and may no longer be a relevant indicator of shallow softness. On the opposite, V_{Smin}
177 does provide an indication of the minimum softness, but without any information on
178 the associated thickness. The B_{30} parameter provides an indication on the amount of
179 velocity variation over the top 30 m: it is generally between 0 and 1, 0 corresponding
180 to a constant value, and 1 to a linear dependence on depth (Régnier et al., 2013).
181 The f_{0HV} parameter, which directly provides the frequency below which the site
182 amplification is negligible (in linear regime), also informs jointly about the softness
183 and thickness over the seismic bedrock (the larger the thickness and/or the lower the
184 softness, the lower the f_{0HV} frequency). The associated A_{0HV} amplitude is intended to
185 provide an indication on the impedance contrast between the deep bedrock
186 (controlling the fundamental resonance) of and the overlying sediments.

187 **2.2 Empirical non-linear to linear site response ratio (RSR_{NL})**

188 The database used in Régnier et al., (2016a) was a subset composed of all the
189 accelerometric data recorded between 1996 and 2009 with magnitudes (M_{JMA}) higher
190 than 3 and epicentral distances below 150 km. This initial database has been

191 enhanced with all strong motion recordings obtained from 2010 to 2014 with peak
192 ground accelerations (PGA) higher than 50 cm/s² at the downhole station, and
193 without any criterion on distance. The resulting data set contains more than 47 600
194 recordings with 7738 recordings having a PGA at the surface above 20 cm/s² on 529
195 sites.

196 The processing involves three steps as illustrated in Figure 1: the derivation of the
197 non-linear to linear spectral ratios RSR_{NL} for each site and recording with a surface
198 PGA greater than 20 cm/s², their normalization in the frequency domain, and then the
199 elaboration of specific data sets for each of the seven considered loading parameters
200 (GMIMs).

201

202 **2.2.1 First step: derivation of "raw" RSR_{NL} ratios**

203 The data were processed as explained in Régnier et al., (2013). The site response
204 for each site event was described by the surface to borehole Fourier amplitude
205 Spectrum Ratio (BSR in the following) as defined in Equation 1 (quadratic mean of
206 the horizontal components).

$$207 \quad BSR = \sqrt{\frac{FAS_{EW_{surface}}^2 + FAS_{NS_{surface}}^2}{FAS_{EW_{borehole}}^2 + FAS_{NS_{borehole}}^2}} \quad \text{Eq 1}$$

208 Where, $FAS_{EW_{surface}}$, $FAS_{NS_{surface}}$, $FAS_{EW_{borehole}}$ $FAS_{NS_{borehole}}$, are the smoothed
209 Fourier amplitude spectrum of the East-West, North-South components of the
210 surface and downhole recordings, respectively. The applied smoothing is the Konno-
211 Ohmachi one (Konno and Ohmachi, 1998) with a parameter b equal to 40.

212 The non-linear soil behavior and its impact on site response is then characterized by
 213 the average of the ratio between non-linear and linear BSRs. At a site (i), the non-
 214 linear to linear site response ratio can be calculated for each strong motion event (j),
 215 we called it RSR_{NLij} . It represents the modification of the weak motion BSR resulting
 216 from non-linear soil behavior due to strong motion j. RSR_{NLij} can be defined
 217 according to Equation (2) for all strong events with a surface PGA higher than 20
 218 cm/s^2 , as the ratio between the BSR of the strong event j over the geometrical
 219 average of BSR calculated on weak events (with surface PGA between 0.1 and 10
 220 cm/s^2) at the same site.

$$221 \quad \log_{10}(RSR_{NLij}) = \log_{10}(BSR_{NLj}) - \frac{1}{N_{iw}} \sum_{w=1}^{N_{iw}} \log_{10}(BSR_{iw}) \quad \text{Eq 2}$$

222 Where RSR_{NLij} is the ratio of the non-linear to linear site response for a given site (i)
 223 and a given strong event j, w the index of weak events, N_{iw} the number of weak
 224 events ($N_{iw} \geq 2$) recorded at site i, and BSR the borehole spectral ratio. As discussed
 225 in Régnier et al. (2016a), the so-defined RSR_{NLij} ratios are considered to characterize
 226 the modification of site response linked to the non-linear behaviour of soft deposits,
 227 whatever the nature of the reference site (i.e., with a sensor at the surface of an
 228 outcropping rock, or at depth within a bore-hole).

229 An average of the RSR_{NLij} over all strong events corresponding to surface PGA
 230 values exceeding a given threshold, or falling within a given range, may then be
 231 calculated, together with the corresponding variability. As described in Régnier et al.,
 232 (2016a), the average RSR_{NL} (Figure 2 (B1)) curves obtained for different PGA
 233 thresholds exhibit a typical frequency dependence close to the first derivative of a
 234 Gaussian function, consisting in three main parts. The first part is a slow increase

235 from one at low frequency until a specific frequency that varies from one site to
236 another. The second part is an abrupt decrease down to values below one. The last
237 part is a slow increase and/or stabilization at values generally below one at high
238 frequency. This shape reflects directly the frequency shift caused by the degradation
239 of elastic properties at large strains, and the increase of damping due to hysteretic
240 behavior. Such a curve is thus characterized by a "pivot" frequency called f_{NL} ,
241 corresponding to the frequency beyond which RSR_{NL} goes below one. This
242 parameter is obviously site specific and could also depend, for a given site, on the
243 loading level, for instance the PGA level at first order. However, Régnier et al.,
244 (2016a) report that such f_{NL} values exhibit almost no dependence on PGA, except for
245 a few thick sites with low fundamental frequency (below 1.5 Hz). In the present study,
246 we have thus assigned to each site the f_{NL} values corresponding to a PGA threshold
247 of 100 cm/s^2 : such a threshold value is large enough to allow a clear NL modulation
248 and an unambiguous pick of the f_{NL} value, and moderate enough to allow a pick for
249 all selected sites. f_{NL} values could be picked automatically for 164 sites, varying from
250 0.49 Hz to 15.7 Hz with a mean value of 5.9 Hz and a standard deviation of 3.7Hz.

251 The RSR_{NL} curves can be considered either in the absolute frequency domain (Step
252 1 of Figure 1), or in a normalized frequency domain, i.e., as a function of the ratio f/f_{NL}
253 (Step 2 of Figure 1). In the absolute frequency domain, the [0.2, 20 Hz] frequency
254 range was subdivided into 49 bins having a constant width on a logarithmic axis, i.e.,
255 corresponding to a constant ratio between central frequencies of two consecutive
256 bins $r = 100^{1/49} = 1.0985$, over which each of the $RSR_{NL}(f)$ curves were averaged.
257 The corresponding central frequencies of each bin are listed in Table B of the

258 Appendix. We are emphasizing that averaging is performed only once in the absolute
259 frequency domain.

260 To develop broad-band models, we kept in our data base only the recordings for
261 which the RSR_{NLij} curve are defined at least for 46 out of the 49 frequency bins, i.e.
262 with a good signal-to-noise ratio (exceeding 3) over almost the whole frequency
263 range [0.2 – 20 Hz].

264 At this stage, the number of RSR_{NLij} data fulfilling all the selection criteria, i.e. (1) a
265 PGA at the surface greater than 20 cm/s^2 , (2) at least two weak events recorded at
266 the same site, (3) a f_{NL} defined at the site and (4) having at most 3 undefined values
267 over the whole range of frequency bins, contains a total of 2927 recordings
268 corresponding to 132 different sites.

269 **2.2.2 Second Step: shift to the normalized frequency domain**

270 Considering the typical shape of RSR_{NL} curves, it was considered useful to also
271 analyse them in a normalized frequency domain, i.e., as a function of f/f_{NL} , so as to
272 better apprehend the sensitivity of this typical shape to loading parameters and site
273 condition proxies. In this aim, we used the f_{NL} values derived for each site as
274 described above. The 49 absolute frequency bins thus resulted into 97 normalized
275 frequency bins, with the central one (bin 49) corresponding to a normalized
276 frequency bin between $0.954 (r^{-0.5})$ and $1.048 (r^{0.5})$. For a site with frequency f_{NL} , the
277 initial absolute frequency bins are simply shifted by $n = 49 - \text{int} \{ \log(f_{NL}/0.2)/\log(r) \}$, so
278 as to automatically assign the central bin 49 to a normalized frequency of 1 and
279 keeping the same ratio $r = 1.0985$ for the width of each normalized frequency bin. For
280 a given site, the range of normalized frequencies thus depends on the f_{NL} value, as it
281 goes from $0.21/f_{NL}$ to $19.1/f_{NL}$, i.e., from bin n to bin $n+48$.

282 **2.2.3 Third step: derivation of "GM-specific" advanced data sets**

283 The "raw, absolute frequency" and "raw, normalized frequency" data established in
284 steps one and two respectively exhibit a significant inhomogeneity in terms of
285 number of recordings per site, and number of recordings per loading level. For
286 instance, the station AKTH04 has 33 recordings, whereas the relatively close
287 AKTH06 station has only five recordings fulfilling the selection criteria. The full range
288 of number of recordings per site goes from 2 to 116. In addition, for every site, the
289 number of recordings is generally much larger for relatively moderate motion than for
290 strong motion. To prevent the statistical models from being biased by the uneven
291 distribution of number of recordings per site and per loading level, we pre-processed
292 the initial data set of RSR_{NL} as described in the following and illustrated in Figure 2.

293 For each of the seven ground-motion intensity measures, we defined 15 bins based
294 on the cumulative distribution functions shown in Figure 2 (A1) for PGA and Figure 3
295 for all GMIMs. We considered 15 bins corresponding to evenly distributed fractiles
296 F_x : every 10% from F10 to F50, and every 5% from F55 to F100. The narrower bins
297 in the 50% upper part of the distribution were designed to discretize more precisely
298 the data corresponding to large loading levels. These are the ranges where soil non-
299 linear behavior is expected to have a larger impact on site response.

300 For each site i , we first count the number of recordings $N_{i,GMk}$ falling in each intensity
301 measure bin k . For example, this number can vary from 0 to 18 in the case we take
302 PGA as GMIM. Therefore, to assign an equal weight to every site in a given intensity
303 measure bin, we take the average of RSR_{NLij} for all the recordings in the bin k . This
304 average is associated to the average ground motion intensity measure of the bin as
305 detailed in Equation (3). It may happen some sites do not have any recording falling

306 in the bin k : $N_{i,GM_k} = 0$. We therefore end up with a total of seven "advanced data
 307 sets" (one for each GMIM : GM in the Eq 3).

$$308 \quad \left[\begin{array}{c} RSR_{NLI-GM_k} \\ \mu_i(GM_k) \end{array} \right]_{GM_k}^{GM_{k+1}} = \left[\begin{array}{c} \frac{I}{N_{i,GM_k}} \sum_{j=1}^{N_{i,GM_k}} RSR_{NLij} \\ \frac{I}{N_{i,GM_k}} \sum_{j=1}^{N_{i,GM_k}} GM_{ij} \end{array} \right]_{GM_k}^{GM_{k+1}} \quad \text{Eq 3}$$

309 Where RSR_{NLI-GM_k} is the average non-linear modulation function for all the recordings
 310 in a bin k and for a site i . The bin is characterized by these limits $bin_k = [GM_k$ to
 311 $GM_{k+1}]$. GM_k varies from $F10(GM)$ for $k=1$ to $F100(GM)$ for $k=15$. N_{i,GM_k} is the number
 312 of records in the same bin at site i . Furthermore, $\mu_i(GM_k)$ is the average GMIM value
 313 between GM_k and GM_{k+1} and for site i ; it is of course bounded by the values GM_k
 314 and GM_{k+1} , and does not vary much from site to site.

315 The procedure is illustrated in Figure 2 for the PGA loading GMIM. The subplot A1
 316 displays the PGA cumulative distribution function for all the recordings. The subplot
 317 A2 shows the total number of sites considered for each PGA bin, while the subplot
 318 A3 refines the number of available sites as a function of f/f_{NL} , again for each PGA bin.
 319 We can observe on subplot A2 that the number of sites does not vary too much from
 320 one PGA bin to another indicating an adequate distribution of the data for a statistical
 321 analysis. The smaller number of sites at low and high normalized frequencies
 322 indicated by subplot A3 has two origins: (1) the original RSR_{NL-GM} , for a given site
 323 and bin, may not be valid over the whole $[0.2-20 \text{ Hz}]$ frequency range because of too
 324 small signal-to-noise ratio and (2) the f_{NL} is variable from one site to another which
 325 results in a site-to-site variability of the available normalized frequency range. That is
 326 why all curves in subplot A3 exhibit a bell shape with a maximum for normalized

327 frequencies close to 1, the values of which correspond to numbers displayed in
328 subplot A2 and varying from 67 to almost 108 sites. Table A in the appendix provides
329 the number of records and the number of sites for each of the 15 intensity bins of the
330 seven intensity measures (instead of only PGA in Figure 2). As expected from the
331 construction of each data set, the number of records in each bin is around 290 in
332 each of the 5 first bins, and half of it, i.e around 145, in the last 10 bins, which
333 correspond exactly to 10% and 5% of the total number of recordings (2927). The
334 number of sites from which the average and standard deviation of the RSR_{NL-GM} is
335 calculated is more variable from bin to bin and GMIM to GMIM, but corresponds to an
336 average of around 90 sites for the first 5 bins, and 70 for the last 10. These numbers
337 are large enough to ensure a statistical significance in each intensity bin, and we
338 therefore consider that these seven advanced data sets are appropriate for
339 investigating the dependency of the RSR_{NL} modulation function as a function of the
340 above listed site condition proxies and intensity measures.

341 As an example, subplots (B1) and (B2) of Figure 2 display, respectively, the average
342 and the standard deviation of all the available RSR_{NL-GM} for each PGA bin, as a
343 function of the normalized frequency f/f_{NL} . These plots are briefly discussed in the
344 next section.

345 **2.3 Statistical overview of the seven data sets**

346 ***2.3.1 Distribution of metadata***

347 The cumulative distributions of the GMIMs and SCPs are displayed on Figures 3, 4
348 and their cross-correlations in Figures 5 and 6. The Figure 3 represents the
349 cumulative distribution function (CDF) of the log values of PGA, PGV, CAV, I_A , D_T ,

350 A_{rms} and PGV/V_{S30} , for the whole set of 2927 recordings: all of them are thus found to
351 follow a lognormal distribution. The same findings stand for the distribution of SCPs
352 (Figure 4), except for B_{30} that follows an approximately normal distribution. Similar
353 distributions are obtained for the three sets of data obtained in step 1, 2 and 3, so we
354 used the logarithm (base 10) values of all GMIMs and SCPs (except for B_{30}) as input
355 for all ANN models. Figure 5 displays the cross-correlations for each pair of GMIMs,
356 together with the corresponding correlation coefficient values. Some pairs exhibit a
357 strong correlation (e.g. $R(PGA, A_{rms}) = 0.96$; or $R(I_A, CAV) = 0.95$), and in general all
358 parameters involving amplitude information are significantly and positively correlated.
359 The Trifunac-Brady duration D_T is found the most poorly correlated with all others.
360 The weakest correlation is found between the strain proxy PGV/V_{S30} and D_T with $R =$
361 -0.01 . Such a strong correlation between most amplitude-related GMIMs suggests
362 that one GMIM is probably enough to characterize the dependence of non-linear site
363 response on loading level.

364 Similarly, to check the possible non-independence between the various SCPs,
365 correlation plots are displayed for each pair of SCPs (Figure 6) together with the
366 corresponding correlation coefficient (R). Another parameter is considered in these
367 plots, the " F_{NL} " frequency, to investigate its possible correlation with the SCPs. Some
368 pairs do exhibit some significant correlation (e.g., $R = 0.65$ for the pair V_{S30-f_0} , $R=0.6$
369 for $V_{S30}-V_{Smin}$), but in general the correlations values are much smaller compared to
370 the various GMIMs, with the weakest correlations corresponding to the $V_{Smin}-B_{30}$,
371 $V_{Smin}-A_{0HV}$ and $V_{S30}-A_{0HV}$ pairs. The SCPs can be considered as almost independent
372 site parameters for the derived ANN models, which allows using more than one SCP
373 in the ANN models.

374 The last column of Figure 6 displaying the correlation plots between f_{NL} and all the
375 considered SCPs is interesting in two respect: the best correlation is found with V_{S30}
376 ($R=0.64$), and the f_{0HV} - f_{NL} scatter plot displays a triangular distribution indicating that
377 f_{NL} is at least equal to, but may be much larger than f_{0HV} , especially for low frequency
378 (thick and/or soft) sites.

379 **2.3.2 Variability of RSR_{NL-GM}**

380 In the normalized frequency domain, the variability of the advanced data sets (Eq. 7)
381 is illustrated in Figure 7 (a). The average variability is similar whatever the intensity
382 measure: it is very low at frequencies below f_{NL} (because all RSR_{NL-GM} ratios are very
383 close to 1 whatever the intensity level), it then steadily increases up to a value
384 around 0.1 (corresponding to around 26% = $(10^{(0.1)}-1).100$) for a unit normalized
385 frequency, and then, after a very narrow-band drop around $f/f_{NL}=1$, stabilizes around
386 a constant value of 0.12 (32%), for $f/f_{NL} > 1$. For some GMIMs, the variability
387 increases for high normalized frequencies (beyond $f/f_{NL}=2-3$), as a result of a larger
388 GMIM bin-to-bin variability and site-to-site variability (see Figure 2B). The drop
389 around $f/f_{NL}=1$ is due to the fact that RSR_{NL-GM} is close to 1 for $f = f_{NL}$; however, the
390 variability does not go down to zero because f_{NL} may change slightly from one
391 intensity bin to the other (in addition to the fact that RSR_{NL-GM} is not exactly equal to 1
392 in the central bin because of the bin averaging process).

393 In the absolute frequency domain (figure 7b), the variability of such RSR_{NL-GM} values
394 is limited at low frequency (typically less than 0.04 log10 – less than 10% - for $f < 0.8$
395 Hz), then is steadily increasing up to a level around 0.17 (i.e. around 48 %) up to a
396 frequency around 10 Hz, beyond which it decreases down to around 0.12 (i.e. around
397 32%) at 20 Hz (the largest considered frequency).

398 While the f_{NL} frequency normalization alone does not allow to significantly reduce the
399 overall scatter of the non-linear modulation function RSR_{NL} compared to the absolute
400 frequency domain, it however allows to better display the main trend in the
401 dependency of RSR_{NL} as a function of the loading intensity level. For instance, the
402 subplot B1 of Figure 2 display, on the example of the PGA, the increase in the
403 modulation function with loading level, with larger low-frequency ($f < f_{NL}$) amplification
404 increase for larger PGA, and larger high-frequency ($f > f_{NL}$) reduction for large PGA.
405 Indeed, below $f/f_{NL} = 1$ the average ratio RSR_{NL} increases until the value of 1.5 for the
406 last PGA bin ($[265-1050[$ cm/s²), while above $f/f_{NL} = 1$, it decreases down to values
407 below 0.5. In addition, the subplot B2 shows that the within-bin variability of all "raw"
408 $RSR_{NLij-GMk}$ ratios exhibits also a significant increase with increasing loading level,
409 with their standard deviation $\sigma_{RSR_{NLij-GMk}}$ slightly exceeding 0.165 (40%) for the last
410 PGA bin below f_{NL} , and reaching up to 0.25 (78%) beyond f_{NL} : it indicates that the
411 non-linear transfer function could be twice the linear one at low frequency, and could
412 be three to four times weaker at high frequency. The loading dependency of the
413 variability (subplot B2) also suggests that other parameters (such as site proxies)
414 could be used to further refine the model and reduce this variability.

415 A similar analysis was conducted with alternative intensity measures such as the
416 strain proxy parameter PGV/V_{S30} : the overall trends are similar but generally less
417 clear.

418 **3 METHODOLOGY**

419 **3.1 Overview**

420 The main aim of this study is two-fold: 1) Investigating the ability of various GMIMs
421 and SCPs to improve the prediction of RSR_{NL-GM} (this will be developed in the
422 sensitivity analysis section), and 2) selecting optimal selection of GMIM and SCPs to
423 derive a RSR_{NL-GM} model allowing to estimate the nonlinear site response from the
424 linear site response. The latter can be obtained inter alia by linear GMPEs in generic
425 studies, or by more detailed, numerical or instrumental, investigations in site-specific
426 studies.

427 To reach the first goal, we use the seven "advanced " datasets developed in the
428 previous section (step 03) and a neural network approach for developing RSR_{NL-GM}
429 prediction equations in the normalized frequency domain, in the mathematical form
430 described in the Equation 4:

$$431 \quad \log_{10} \left[RSR_{NL-GM} (f / f_{NL}) \right] = G(\beta | (W, b)) \pm \varepsilon \cdot \sigma (f / f_{NL}) \quad \text{Eq.4}$$

432 where

- 433 • G is the prediction functional form,
- 434 • σ represents the standard deviation of residuals, and ε is representing the
435 residual normalized by σ .
- 436 • β designates the GMIM vector and the SCP matrix
- 437 • W and b represent the parameters of the neuronal model which are tuned to
438 optimize the fit as described in the next section.

439 • Given the range of values of f_{NL} [0.49 – 15.7 Hz], the normalized frequency $\nu =$
440 f/f_{NL} is ranging from around 0.015 to 40, with however only few values at the
441 two extremities of this interval (see Figure 2, subplot A3).

442 The neuronal model has the advantage of not requiring a prior functional form
443 (Derras et al., 2012): the actual dependence is established directly from the data and
444 can therefore be used as a guide for a better understanding of the factors that control
445 ground motions.

446 The results obtained in the sensitivity analysis will be later used to establish the final
447 RSR_{NL-GM} equation in the absolute frequency domain, in an analogous form as
448 shown in Equation 5

$$449 \quad \log_{10} \left[RSR_{NL-GM}(f) \right] = H(\beta | (W, b)) \pm \epsilon \cdot \sigma(f) \quad \text{Eq.5}$$

450 **3.2 Artificial Neural Network Methods approach**

451 An ANN is made up with interconnecting artificial neurons within input, hidden and
452 output layers. The symbols W and b represent the synaptic weights and bias with
453 subscripts representing the corresponding neurons, respectively (Figure 8). The ANN
454 type used in this work is the feed-forward ANN (Hu and Hwang, 2002).

455 The Quasi-Newton Back Propagation technique also called “BFGS” (Robitaille et
456 al., 1996) has been used in this work for the training phase. This method considers
457 the second derivatives with respect to the unknown coefficients of the input-output
458 relationship and is therefore more efficient than the original method of back-
459 propagation. The number of iterations required to converge is significantly lower and
460 the computation time is reduced (Demuth et al., 2009).

461 The performances of the results obtained by ANN are measured by the standard
 462 deviation σ of residuals between observations and model predictions (Eq.6),
 463 compared to the standard deviation σ_{ref} of the original advanced data set (Eq.7)
 464 through the variance reduction coefficient R_c as defined in Eq. 8

$$465 \quad \sigma = \sqrt{\frac{1}{M} \sum_1^M (\log_{10}(RSR_{NL-GM,obs}) - \log_{10}(RSR_{NL-GM,pred}))^2} \quad \text{Eq 6}$$

$$466 \quad \sigma_{ref} = \sqrt{\frac{1}{M} \sum_1^M (\log_{10}(RSR_{NL-GM,obs}) - \log_{10}(\text{mean}(RSR_{NL-GM,obs})))^2} \quad \text{Eq.7}$$

$$467 \quad R_c = (1 - \frac{\sigma^2}{\sigma_{ref}^2}) \cdot 100 \quad (\%) \quad \text{Eq.8}$$

468 where $RSR_{NL-GM,obs}$ represents the "observed" RSR_{NL-GM} as derived in the step 3
 469 advanced data set. $RSR_{NL-GM,pred}$ is the neural prediction of the RSR_{NL-GM} (either in
 470 the normalized frequency domain for the sensitivity study, or in the absolute
 471 frequency domain for the final model). M is the size of the advanced data set.

472 Using an ANN method, the residual error can be driven to a very small value, for
 473 instance through the use of a large number of nodes in the hidden layer. However,
 474 when new data are presented to the network the resulting error may become large.
 475 To avoid it, the regularization method is used in this study. This method involves
 476 modifying the conventional mean sum of squares of the network errors by adding a
 477 term equal to the mean of the sum of squares of the network weights and biases
 478 (Derras et al, 2012), which de facto limits the number of degrees of freedom.

479 **3.3 Design of ANN model**

480 The design of the ANN model requires several choices regarding:

- 481 • the input parameters (here GMIMs and SCPs) which are relevant for
- 482 explaining the variability of output responses (in this study RSR_{NL-GM}),
- 483 • the number of hidden layers,
- 484 • the corresponding number of neurons,
- 485 • the selection of the activation functions.

486 We first have chosen the number and the kind of independent parameters of our
487 predictive models (inputs of the neural model): this is the main topic addressed in the
488 sensitivity study described in the next section. A single hidden layer has been finally
489 systematically selected for all models (Figure 8). Two or more hidden layers would
490 have allowed to reach much smaller errors, but it would also have significantly
491 increased the complexity of the model, raising the issue of an “over-fitting”: such
492 models are not favored by the regularization technique. In addition, an ANN model
493 with one single hidden layer has been shown to be a universal function approximator
494 (Wolfgang 1997; Peter et al., 2008).

495 Here, the number of neurons in this single hidden layer (N) has been taken equal to
496 the number of the independent parameters considered in the input layer (Wierenga
497 and Kluytmans, 1994). This choice allows to reach an optimal compromise between
498 σ reduction and Akaike Information Criterion (AIC) increase due to larger number of
499 degrees of freedom.

500 Several activation functions (between input and hidden layers and between hidden
501 and output layers) have been considered. The lowest σ value, and the lowest number
502 of iterations as well, have been obtained with a hyperbolic tangent function for the
503 former, and a linear one for the latter (their schematic shape is shown in Figure 8). All

504 the tests and the final implementation have been performed with the Matlab Neural
505 Network Toolbox™ (Demuth et al., 2009).

506 The final neural models thus consist of a series of three layers. The first represents N
507 inputs, (one GMIM and {N-1} SCPs). The second, hidden layer has the same number
508 N of neurons. The last layer represents the values of RSR_{NL-GM} for 97 normalized
509 frequency bins (sensitivity analysis), or 49 absolute frequency bins (final model). The
510 selected architecture is therefore of the N-N-97 or N-N-49 type.

511 **4 Normalized frequency domain: results and sensitivity**

512 **analysis**

513 **4.1 Outline**

514 To investigate the respective performance of the various GMIMs and SCPs in
515 predicting the non-linear modulation, i.e., in reducing the model residual, different
516 $RSR_{NL-GM}(f/f_{NL})$ ANN-models were built. A schematic description is given in Figure 1
517 (step 4). Their performance is evaluated for each normalized frequency through the
518 variance reduction coefficient $R_c(f/f_{NL})$ (Eq.8). This frequency dependent quantity
519 describes the capacity of the model to explain the observations. Figure 9 displays the
520 R_c values as a function of the normalized frequency f/f_{NL} for several one or two-input
521 parameter models, considering either one GMIM, or the combination of each GMIM
522 with one of the five SCPs. The variance reduction is found to exhibit significant
523 differences from model to model, and also significant variations with normalized
524 frequency: the variance reduction is very small for (f/f_{NL}) values much smaller than 1,
525 it then increases and reaches a maximum R_{cmax} for f/f_{NL} between 1 and 2, and

526 stabilizes around an almost constant value (model-dependent, and generally ranging
527 from 5% to 15%), for f/f_{NL} values beyond 3 to 5. One may also notice the sharp and
528 narrow drop of R_c for f/f_{NL} around 1 (with R_c values most often between 3% and 8%).
529 This drop is related to the definition of f_{NL} : all RSR_{NL-GM} values are very close to 1, the
530 initial variance is already very small (see Figure 2: B2) and the models cannot reduce
531 it further.

532 Amongst the one-GMIM models, one can observe that the performance ranking also
533 exhibits a slight dependence on the normalized frequency. The Trifunac-Brady
534 duration has a low performance, the best performances are achieved by ground
535 motion amplitude related parameter such as PGA, PGV, I_A and A_{rms} , and
536 intermediate performances are observed for CAV and strain proxy PGV/V_{S30} . Such
537 one-GMIM models reduce the variance by at most 25-30% around f_{NL} , and around
538 10% at high frequencies. When adding one SCP to a GMIM, the prediction is
539 significantly improved for $f/f_{NL} \geq 1$, with R_{cmax} exceeding 30%, and a slight trend to a
540 lower model-to-model differentiation at high frequency, to the exception of all those
541 involving the Trifunac-Brady duration, which still perform very poorly. The
542 performance is significantly improved when the SCP is V_{S30} , f_{0HV} or B_{30} , and for the
543 strain proxy PGV/V_{S30} when associated to any additional SCP (especially V_{S30} or
544 f_{0HV}). This result was expected as the SCPs (essentially V_{S30}) are used in GMPEs to
545 model the non-linear component of site response.

546 **4.2 Quantitative Model Ranking**

547 Figure 9 indicates that the area where GMIM and SCP mostly contribute to the
548 reduction of the variability and exhibit the largest model-to-model differences,
549 corresponds to f/f_{NL} around one (just below and above f_{NI}). It was thus decided to

550 characterize the performance of each ANN model by a single, scalar value,
551 corresponding to the arithmetic mean $\mu(R_c)$ over the normalized frequency range
552 [0.25-4.0]. The $\mu(R_c)$ values are listed on Table 1 and displayed in Figure 10,
553 indicating that the best GMIMs, when considered without any SCP, are, quite
554 surprisingly, those related with acceleration amplitude: $\mu(R_c)$ values are 13.2% and
555 12.7% for PGA and A_{rms} , respectively. Those involving mid-frequency information (I_A ,
556 PGV and CAV) exhibit a slightly lower performance (10.7%, 10.1% and 7.8 %,
557 respectively), while PGV/ V_{S30} performs very modestly ($\mu(R_c)= 5.4\%$), and duration D_T
558 very poorly (1.9%).

559 These average variance reduction values are significantly improved when adding one
560 SCP, as shown in Table 1 and Figure 10. This improvement is most noticeable when
561 using PGV/ V_{S30} , for which $\mu(R_c)$ increases from 5.4% to an average value of 11.4 %,
562 and up to 15.9% when using the V_{S30} SCP. One may notice also that the
563 performance remains very poor for the duration D_T : $\mu(R_c)$ is less than 6% whatever
564 the considered site proxy, which indicates that NL behavior should definitely be
565 related with some amplitude measure (incidentally, one may also notice that for D_T ,
566 the best improvement is found when considering the " A_{0HV} " site proxy, i.e. the only
567 one directly related with some amplitude information). For all other GMIMs, the single
568 site proxy leading to the best performance is almost systematically the site
569 fundamental frequency. The best one-GMIM one-SCP combination is found to be
570 (PGV, f_{0HV}) with a mean variance reduction of 16.4%, and the two other best
571 combinations are found to be [PGA; f_{0HV}] and [A_{rms} ; f_{0HV}] with mean variance

572 reductions of 15.7% and 15.3%, respectively. On the opposite, the site proxy leading
573 to the worst performance is almost systematically the minimum S-wave velocity V_{Smin} .
574 Model performances are improved when considering more SCPs in the input layer,
575 as listed in Table 1 and Figure 10. One may notice however that the improvements
576 are more and more marginal as the number of input SCPs is increased: when
577 considering all SCPs together, the mean variance reduction $\mu(R_c)$ always remain
578 below 20%, which may be interpreted as an indication of the limited relevancy of all
579 the considered site proxies for a physical characterization of the non-linear site
580 response. Other parameters such as plasticity index, relative density, fine contents
581 could be more relevant, but unfortunately are not available as site metadata in any of
582 the strong motion data repositories. That is why we have not considered all possible
583 combinations but have limited to all [one-GMIM, two SCPs] models, and a few more
584 with best performing three and four SCP models.

585 Table 1 and figure 10 call for several specific comments:

- 586 • The GMIM leading to best performance within all [one-GMIM, two SCPs]
587 models and all [one-GMIM, all SCPs] models are the strain proxy PGV/V_{S30}
588 with $\mu(R_c)$ values of 19.76 % in the latter case, and above 18% for the two-
589 SCP combinations (V_{S30}, f_{0HV}) , (V_{S30}, B_{30}) , and (V_{S30}, A_{0HV}) (18.59, 18.47 and
590 18.16%, respectively).
- 591 • The other GMIM leading to variance reduction above 17% are PGV, when
592 associated to f_{0HV} and A_{0HV} (17.50%), or f_{0HV} and V_{S30} (17.260%), or V_{S30} and
593 B_{30} (17.01%), or f_{0HV} and B_{30} (17.0%), and PGA, when associated to B_{30} and
594 A_{0HV} (17.19%). In average thus, peak values (PGV/V_{S30} , PGA and PGV) better

595 explain the NL modulation of site response than other intensity measures also
596 accounting for duration (I_A , CAV, A_{rms} , D_T).

597 • Regarding the SCPs, one may notice the frequent presence of V_{S30} , f_{0HV} , and
598 B_{30} within the best performing (one-GMIM, two SCPs) models listed above
599 (i.e., $\mu(R_c)$ values above 17 %). As the first two are already known to provide
600 best performing models for linear site amplifications (NGA-West 2; RESORCE
601 Douglas 2014; Boudghene-Stambouli et al., 2017; Derras et al., 2016, 2017),
602 it is interesting to notice that instrumental data – without any modelling as in
603 NGA-West 2 – do support their usefulness also for NL behavior. The
604 appearance of the B_{30} SCP is not surprising since B_{30} characterizes the
605 shallow velocity gradient, and large gradients, associated to large impedance
606 contrasts near the surface, are likely to generate high strains and thus
607 significant NL modifications (see Régnier et al., 2013). This parameter is
608 however not available in most strong motion database and the use of models
609 involving B_{30} is thus probably premature. Even though measuring B_{30} is
610 definitely less simple and reliable than measuring f_{0HV} , it would be however
611 useful to investigate the feasibility of its measurement from non-invasive
612 techniques (as for V_{S30}), for future developments.

613 From all these results, we can thus recommend the use of PGA as a relevant
614 shaking intensity measure controlling the nonlinear modulation of site response in the
615 case no site proxies are available. In the opposite case, which is fortunately more
616 and more frequent, the present results lead to recommend the use of PGV/ V_{S30} for
617 NL site response models; PGA or PGV based models do have however a quite
618 satisfactory performance.

619 In summary, the optimal [GMIM, two-SCPs] combinations providing the largest
620 variance reductions are the triplets [PGV/ V_{S30} , $V_{S30-f_{0HV}}$] ($R_c = 18.6\%$), [PGV/ V_{S30} ,
621 $V_{S30-A_{0HV}}$] ($R_c = 18.2\%$), [PGV, $V_{S30-f_{0HV}}$] ($R_c = 17.3\%$) and [PGA, $B_{30-A_{0HV}}$] ($R_c =$
622 17.2%).

623 For the best [PGV/ V_{S30} , $V_{S30-f_{0HV}}$] model, the details on variance reduction displayed
624 on Figure 11 indicate that the peak reduction R_{cmax} is about 40% and occurs for
625 normalized frequency between 1 and 2: despite the relatively moderate value of
626 mean variance reduction over the whole interval [0.25-4.0], this peak value
627 emphasizes the interest of this model especially in the frequency range where linear
628 site amplification is significant.

629 **5 Final model: Absolute frequency domain**

630 The sensitivity study of the previous section allowed to identify the optimal input
631 parameters regarding the shaking intensity level and the site-condition proxies.
632 However, it was performed in the normalized frequency domain, and the f_{NL}
633 frequency is site-specific and cannot be simply predicted: an attempt to relate f_{NL}
634 directly to SCs through a similar ANN approach yielded poorly performing models.
635 Therefore, to develop a tractable model for practical applications, it was decided to
636 take advantage of the normalized frequency sensitivity study to select the optimal
637 triplet (PGV/ V_{S30} , V_{S30} , f_{0HV}), and to develop a new ANN model in the absolute
638 frequency model. This section is devoted to a presentation of this new model, and to
639 a discussion of its results. In such a model, V_{S30} provides an indication on the
640 stiffness of the site at shallow depth, while f_{0HV} provides a combined information on
641 the overall stiffness and thickness of the whole soil column down to the bedrock.

642 **5.1 The KiK-net ANN (PGV/V_{S30}, V_{S30}, f_{0HV}): functional form**

643 We considered the same, simple neural network architecture as illustrated in Figure
644 8, and applied to the PGV/V_{S30} advanced data set to predict the dependence of
645 RSR_{NL} as a function of PGV/V_{S30}, V_{S30} and f_{0HV}. It thus results in a relatively simple,
646 data-driven functional form, providing the estimation in log₁₀ (RSR_{NL-GM} (f)) over the
647 [0.2–20] Hz frequency range through the Equation 9.

$$648 \quad \log_{10} [RSR_{NL-GM} (f)] = C1(f).F1 + C2(f).F2 + C3(f).F3 + C4(f) \text{ Eq.9}$$

649 Where:

$$650 \quad \begin{cases} F1 = \tanh(-0.908 + 0.492.\log_{10}(V_{S30}) - 0.352.\log_{10}(f_{0HV}) + 0.097.\log_{10}(PGV / V_{S30})) \\ F2 = \tanh(-2.477 + 1.01.\text{Log}_{10}(V_{S30}) + 0.448.\text{Log}_{10}(f_{0HV}) + 0.274.\text{Log}_{10}(PGV / V_{S30})) \\ F3 = \tanh(-1.595 + 0.216.\text{Log}_{10}(V_{S30}) - 0.092.\text{Log}_{10}(f_{0HV}) - 0.710.\text{Log}_{10}(PGV / V_{S30})) \end{cases}$$

651 The *tanh* dependency is related to the selection of the Tanh-sigmoid activation
652 function for the hidden layer (see Figure 8). The frequency dependent coefficients C1
653 to C4 are listed in Table B of the Appendix, together with the standard deviation
654 $\sigma_{\log_{10}(RSR_{LN-GM}(f))}$ and the variance reduction coefficient $R_c(f)$.

655 **5.2 Residual analysis**

656 The ANN model is obtained here also using the training-regularization (Derras et al,
657 2012) procedure. In addition to the median, the ANN approach gives also the
658 aleatory uncertainty part (Eq. 5).

659 The first check of the ANN model consists of an analysis of the distribution of the
660 residuals (eq.10).

$$661 \quad \text{Residuals}(f) = \log_{10}(RSR_{NL-GM,obs}(f)) - \log_{10}(RSR_{NL-GM,pred}(f)) \text{ Eq.10}$$

662 Where $RSR_{NL-GM,obs}$ and $RSR_{NL-GM,pred}$ are the recorded and predicted values
663 respectively, for a given site and ground motion bin.

664 These residuals are found to approximately follow a lognormal distribution, and to be
665 free from any systematic trend (bias) versus any of the three input parameters
666 PGV/V_{S30} , V_{S30} and f_{0HV} . Figure 12 displays the distribution of residuals average and
667 $\pm \sigma$ per bin versus V_{S30} , f_{0HV} and PGV/V_{S30} for two frequencies, 2.4 and 8 Hz,
668 corresponding respectively to the 20% and 80% fractiles of the f_{NL} cumulative
669 distribution functions displayed in Figure 4. Each parameter bin has been selected to
670 include about 100 data points in order for the statistics to be significant. For
671 PGV/V_{S30} , it should be noted that the bins used for the Figure 12 plot are not the
672 same as those used for building the advanced dataset in step 3. While the mean of
673 residuals within each SCP bin does vary from bin to bin, these variations do not
674 exhibit any systematic trend or bias, as the mean values remain within the $\pm 1 \sigma$
675 interval whatever the considered bin and the considered input parameter. One may
676 notice in particular that the model behaves better with PGV/V_{S30} (very flat mean
677 curve, with values close to 0) than with V_{S30} and f_{0HV} (exhibiting some erratic though
678 limited variability). This is normal since PGV/V_{S30} is the parameter which is used to
679 transform the initial data into equally distributed ranges for optimally analysing the
680 effect of shaking intensity on NL modulation.

681 As complementary information to the effects of the GMIM and SCPs on aleatory
682 variability, the total percentages of synaptic weight, P_i (%) corresponding to each of
683 the three input parameters were computed as explained in Derras et al., (2012)
684 (Equation 10). These synaptic weights assign the largest contribution to PGV/V_{S30} (57
685 %), while the two SCPs V_{S30} and f_{0HV} contribute almost equally (23% and 20%,
686 respectively).

687 **5.3 Example RSR_{NL-GM} ANN predictions**

688 Figure 13 displays some example RSR_{NL-GM} predictions by the final ANN model. The
689 estimation is performed for different levels of PGV/V_{S30} (as in Figure 2) and for 6 soil
690 profiles cases. We have chosen the values of the couples (V_{S30}, f_{0HV}) so as they
691 satisfactorily span the range of values of the initial data set, while remaining in the
692 core of the data set (see Figure 6 and the insert in Figure 13A). The 6 cases
693 considered for Figure 13 include a soft, low frequency site (160 m/s, 0.3 Hz, case A),
694 three sites with a constant, intermediate shallow stiffness ($V_{S30} = 300$ m/s) with low to
695 intermediate fundamental frequency (0.3, 1 and 3 Hz for cases B, C and D,
696 respectively), and finally two stiff sites ($V_{S30} = 800$ m/s) with intermediate to high
697 fundamental frequency (3 and 9 Hz, respectively).

698 Figure 13 calls for several comments:

- 699 a) As expected from the original RSR_{NL-GM} observations (like Figure 2 (B1)), the
700 predicted RSR_{NL-GM} exhibits the classical shape with a low frequency part above 1
701 and a high-frequency part below 1.
- 702 b) The impact of soil non-linear behavior increases with the strain proxy level: the
703 low frequency over-amplification reaches value of 1.25 for large PGV/V_{S30} values
704 (bin [0.0351%-0.5829%], while the high-frequency reduction also increases with
705 increasing PGV/V_{S30} . At high frequency (beyond f_{NL}) the non-linear transfer
706 function could be three times weaker.
- 707 c) The comparison of predictions for stiff sites and softer sites also suggest larger
708 NL changes for stiff sites. This is relatively surprising, but actually, such an
709 unexpected result has been already reported in Régnier et al., (2016b): the most
710 likely interpretation is that sites with relatively large V_{S30} and f_{0HV} most often

711 consist of thin, softer layers resting on much harder rock (also leading to high-
712 frequency amplification, as shown by Laurendeau et al., 2018): the associated
713 large impedance contrast may thus result, under strong shaking, in large strains,
714 and therefore in significant NL effects.

715 d) Another apparently surprising observation is the appearance of non-linearity even
716 at low levels of strain: even the curves corresponding the first three to four
717 PGV/ V_{S30} bins exhibit some low-frequency bump and high-frequency trough. One
718 must keep in mind however that all sites, even in the linear domain, present a
719 significant event-to-event variability in their site response (see for instance
720 Maufroy et al., 2017, for an in-depth discussion of the origins of such a variability).
721 Such a variability may be estimated in Figure 2 with the standard deviation within
722 the smallest PGA bin (solid red curve in panel B2): the high frequency sigma is
723 around 0.08, corresponding to a factor around $\pm 20\%$, Therefore, the median
724 predictions of Figure 13 should always be considered with the uncertainty
725 corresponding to the standard deviation of the model (Table B in the appendix),
726 which increases from about 0.03 around 0.3 Hz (i.e., $\pm 7\%$), to 0.05 around 1 Hz
727 ($\pm 12\%$), and 0.13 around 10 Hz ($\pm 35\%$). The low frequency predictions are more
728 reliable than the high frequency predictions, and all high frequency predictions
729 falling within $\pm 15-20\%$ of the unit value should be interpreted with caution.

730 Figure 14 provides an alternative insight in the model predictions, by showing the
731 changes in predicted RSR_{NL-GM} curves with V_{S30} for fixed values of PGV/ V_{S30} and f_{0HV}
732 (Figure 14A), and with f_{0HV} for fixed values of PGV/ V_{S30} and V_{S30} (Figure 14B). For
733 both cases, the strain proxy is taken equal to relatively large values with significant
734 NL effects (0.02 %, i.e., corresponding to fractile 85-90 in Figure 3), while f_{0HV} is

735 taken equal to 3 Hz in Figure 14A (close to its median value), and V_{S30} to 300 m/s in
736 Figure 14B (corresponding to the 25% fractile value, but relatively close to its median
737 value of 375 m/s, see Figure 3 bottom). The variations of V_{S30} (Figure 14A) and f_{0HV}
738 (Figure 14B) are limited by the reliability range provided by the distribution of original
739 data in the (V_{S30}, f_{0HV}) plane shown in Figure 6: from 300 to 800 m/s for V_{S30} and from
740 0.3 to 9 Hz for f_{0HV} . One may notice again that the NL effects (i.e., the deviation of
741 RSR_{NL-GM} ratio from 1, above and below) increase with site shallow stiffness (V_{S30})
742 and site fundamental frequency f_{0HV} . One may also notice that, at least for the cases
743 considered here centred around the median values of V_{S30} and f_{0HV} , V_{S30} variations
744 are mainly impacting the intermediate to high frequency part [2-10] Hz, while f_{0HV}
745 variations affect a lower frequency band between 1 Hz and 5 Hz. Moreover, f_{NL} is
746 found to increase with increasing V_{S30} and increasing f_{0HV} , which could be expected
747 from the scatter plots of Figure 6: the present ANN model also indirectly offers the
748 possibility to provide an estimate of the pivot frequency f_{NL} . It therefore turns out that,
749 even though their synaptic weights are lower than the one of the strain proxy
750 PGV/V_{S30} , V_{S30} and f_{0HV} are parameters which are useful to be considered for an
751 empirical prediction of nonlinear site response.

752 We thus consider that the derived ANN(PGV/V_{S30} , V_{S30} , f_{0HV}) model proves to be
753 reasonably satisfactory in predicting the nonlinear modulation of site response, and is
754 the one of the very few (together with the GMPE model by Sandikkaya et al., 2013),
755 to be based only on instrumental data. In addition, this model is the only one that
756 takes into account not only of the “classical” high-frequency reduction due to
757 increased damping, but also the low-frequency over-amplification associated with
758 modulus degradation and the resulting shift of the site resonant frequencies.

759 **6 CONCLUSIONS AND DISCUSSION**

760 The present set of investigations based only on instrumental data (a subset of KiK-
761 net recordings) allows to draw interesting conclusions regarding the onset of NL
762 behaviour, the ground motion intensity measures that seem to control the non-
763 linearity of site response, the site proxies which perform the best in predicting the NL
764 modulation of site response and the quantitative dependence of NL modulation on
765 site and loading parameters. In addition, from a methodological viewpoint, the
766 present study emphasizes once again the usefulness of computational statistics tools
767 such as the neural network approach, which does not require any a priori assumption
768 on the functional form of the dependence on the input parameters, and thus allows to
769 test a wide number of combinations, and to choose the most relevant ones on the
770 basis of a simple performance indicator based on variance reduction coefficient.

771 Both the simple statistical analysis of RSR_{NL-GM} ratios grouped in the normalized
772 frequency domain according to increasing loading bins, and the predictions of neural
773 network models indicate the onset of detectable NL site response changes at rather
774 low shaking levels. For instance, Figure 2 indicates a noticeable NL effect at high
775 frequency, from the first PGA bin, i.e., 0.03g, and a significant one at low and high
776 frequency for PGA larger than 0.1g, while example predictions in Figure 13 and 14
777 indicate noticeable high frequency decrease for strain proxy values (PGV/V_{S30}) as
778 low as 0.01%. Nevertheless, the corresponding average changes are smaller than, or
779 comparable to the standard deviations (see Figure 7). This probably explains why
780 such NL effects are difficult to detect and model in usual GMPEs, where the non-
781 linear part of site response variability is mixed with other terms and their variabilities
782 (source, crustal path, linear, generic site term associated to a simple and single site

783 proxy). In any case, this onset of slight non-linearities at rather low loading levels is
784 consistent with recent statistical studies (Guéguen et al., 2019) suggesting that the
785 main recent strong motion data bases (NGA, KiK-net – K-Net, ESM) do include some
786 detectable non-linearities, which, though limited, are found larger than what is
787 predicted by non-linear site terms of recent GMPEs.

788 The ability of various site-condition proxies and ground motion intensity measures to
789 explain the non-linear modulation of site response could be compared through the
790 variance reduction performance coefficient. Even though the results exhibit some
791 changes as a function of the parameter combination, some rather general and robust
792 results may be outlined for the seven intensity measures that were considered:

- 793 • The worst performing one is, as expected, the Trifunac-Brady duration, i.e.,
794 the only one which does not account at all for the shaking amplitude
- 795 • The best performing ones, when associated with other site proxies, are peak
796 values intensity measures, i.e., PGA, PGV and the peak strain proxy
797 PGV/V_{S30} . (Table 1). It is worth noticing however that the latter performs well
798 only when associated to two site proxies. When considered individually to
799 predict RSR_{NL-GM} in the normalized frequency domain, it surprisingly performs
800 very poorly, while when associated with one single site proxy, it performs well
801 only with V_{S30} or f_{0HV} , unlike PGA and PGV which perform well with all site
802 proxies. We do not have any tentative explanation for such a result, which
803 may however indicate that this quantity is only a rather crude proxy to the
804 peak strain, for which the best reference velocity could be the minimum
805 velocity instead of V_{S30} .
- 806 • Intensity measures mixing amplitude and duration (I_A , CAV and A_{rms}) exhibit an
807 intermediate performance, with a significantly better one however for the latter.

808

809 Three groups of site proxies may also be identified according to their ability to
810 predict the non-linear modulation of site response, again with the use of the same
811 performance indicators.

812 • The best SCPs providing the largest variance reduction are found to be the
813 classical shallow velocity proxy V_{S30} and the fundamental frequency f_{0HV} .

814 • The shallow gradient indicator B_{30} proves to perform rather well. However,
815 since its estimation requires the knowledge of the velocity profile over the top
816 30 m (which is not required neither for f_{0HV} nor for V_{S30} , at least when the
817 latter is estimated from surface wave dispersion curves), it is probably more
818 efficient in the next years to prefer the two previous site proxies, especially as
819 the latter have proved to perform well in predicting linear site amplification
820 (Boudghène-Stambouli et al., 2017; Derras et al., 2017; Hassani and Atkison,
821 2016, 2018)

822 • The worst performing site proxies are the minimum velocity V_{Smin} and the
823 fundamental peak amplitude A_{0HV} . None of them however are commonly used
824 as site proxies in GMPEs.

825 As a result, the most effective combination of GMIM and SCP to predict non-linear
826 modulation of site response was found to be the strain proxy PGV/V_{S30} and the two
827 complementary site proxies V_{S30} and f_{0HV} , which provide a variance reduction of
828 18.6% in the normalized frequency domain, and of about 26% in the absolute
829 frequency domain. The latter, in addition to its improved performance with respect to
830 the normalized frequency domain, offers the advantage to avoid the need to find a
831 parallel way predict the pivot frequency f_{NL} . Such a model could thus be used to
832 obtain a first level estimation of the impact of soil non-linearities on site response,

833 whatever the method followed to estimate the linear site amplification (generic with
834 some GMPE, or site-specific using instrumental recordings or numerical simulation).
835 Further developments on this approach are nevertheless needed to better
836 understand what are the parameters which control the value of f_{NL} (which is always
837 larger than, or equal to, f_{0HV} , see Figure 6), and whether it may always be considered
838 as approximately independent of the loading intensity (as we assumed here). An
839 interesting direction of research might be to consider, for the same KiK-Net data
840 subset, the differences between the fundamental frequency f_{0HV} , and the dominant
841 site response frequency f_{peak} (Hassani and Atkinson, 2016). Another one would be to
842 perform the same kind of analysis on comprehensive sets of well controlled, 1D non-
843 linear numerical simulations, in order to identify the possible control by other, more
844 refined (and less easily available) soil parameters such as the plasticity index or the
845 reference strain γ_{ref} (strain at which the shear modulus is reduced by 50%).

846 **7 DATA AND RESOURCES**

847 Time histories and velocity profiles used in this study were collected from the KiK-Net
848 web site www.kik.bosai.go.jp and <http://www.kik.bosai.go.jp/kik/> (last accessed
849 October 2014).

850 **8 ACKNOWLEDGEMENTS**

851 First, we thank two anonymous reviewers for their very detailed comments and
852 constructive criticism that helped us to improve this manuscript. We also
853 acknowledge the support from the TASSILI program and the SINAPS@ project that
854 received French funding managed by the National Research Agency under the
855 program “Future Investments” (Sinaps@ reference: ANR-11-RSNR-0022). Sinaps@
856 is a “Seism Institute” project (<http://www.institut-seism.fr/projets/sinaps/>). The

857 authors are very grateful to NIED for providing such high-quality earthquake
858 recordings.

859 **9 REFERENCES**

- 860 Boudghene-Stambouli, A., Zendagui, D., Bard P-Y., and Derras B., 2017. Deriving
861 amplification factors from simple site parameters using generalized regression
862 neural networks: implications for relevant site proxies, *Earth Planets Space*
863 **69**:99. doi.org/10.1186/s40623-017-0686-3.
- 864 Chandra, J., Guéguen, P., and Bonilla, L.F., 2016. PGA-PGV/Vs considered as a
865 stress– strain proxy for predicting nonlinear soil response, *Soil Dyn Earthq*
866 *Eng* **85**,146–160. doi.org/10.1016/j.soildyn.2016.03.020.
- 867 Demuth, H., Beale, M., and Hagan, M., 2009. Neural Network Toolbox™ 6, User’s
868 Guide. The MathWorks, Inc.
- 869 Derras, B., Bard P-Y., and Cotton, F., 2016. Site-conditions proxies, ground-motion
870 variability and data-driven GMPEs insights from NGA-West 2 and RESORCE
871 datasets. *Earthq Spectra* **32**,2027–2056. doi.org/10.1193/060215EQS082M.
- 872 Derras, B., Bard, P. Y., and Cotton, F., (2017). V_{s30} , slope, H_{800} and f_0 : Performance
873 of various site-condition proxies in reducing ground-motion aleatory variability
874 and predicting non-linear site response, *Earth, Planets and Space*, **69**:133.
875 doi.org/10.1186/s40623-017-0718-z.
- 876 Derras, B., Bard, P-Y., and Cotton, F., 2014. Towards fully data-driven ground motion
877 prediction models for Europe, *Bull. Earthq. Eng* **12**, 495–516.
878 doi.org/10.1007/s10518-013-9481-0.

879 Derras, B., Bard, P-Y., Cotton, F., and Bekkouche, A., 2012. Adapting the neural
880 network approach to PGA prediction: an example based on the KiK-net data,
881 *Bull. Seism. Soc. Am* **102**, 1446–1461. doi.org/10.1785/0120110088.

882 Douglas, J., Akkar, S., Ameri, A., Bard, P-Y., Bindi, D., Bommer, J. J., Bora, S. S.,
883 Cotton, F., Derras, B., Hermkes, M., Kuehn, N. M., Luzi, L., Massa, M., Pacor,
884 F., Riggelsen, C., Sandikkaya, M. A., Scherbaum, F., Stafford, P. J., and
885 Traversa, P., 2014. Comparisons among the five ground-motion models
886 developed using RESORCE for the prediction of response spectral
887 accelerations due to earthquakes in Europe and the Middle East, *Bull. Earthq.*
888 *Eng* **12**, 341-358. doi.org/10.1007/s10518-013-9522-8.

889 Field, E.H., P.A. Johnson, I.A. Beresnev and Y. Zeng., 1997. Nonlinear ground-
890 motion amplification by sediments during the 1994 Northridge earthquake,
891 *Nature* **390**, 599–602. doi.org/10.1038/37586.

892 Fujiwara, H., Aoi, S., Kunugi, T., and Adachi, S., 2004. Strong-motion Observation
893 Networks of NIED: K-NET and KiK-NET, National Research Institute for Earth
894 Science and Disaster Prevention.

895 Guéguen, P., Bonilla, L. F., and Douglas, J., 2019. Comparison of Soil Nonlinearity
896 (In Situ Stress–Strain Relation and G/G_{\max} Reduction) Observed in Strong-
897 Motion Databases and Modeled in Ground-Motion Prediction Equations, *Bull.*
898 *Seismol. Soc. Am* **109**, 178-186. doi.org/10.1785/0120180169.

899 Hassani, B., and Atkinson G.M., 2018. Site Effects Model for Central and Eastern
900 North America Based on Peak Frequency and Average Shear -Wave Velocity,
901 *Bull. Seismol. Soc. Am*, **108**, 338-350. doi.org/10.1785/0120170061.

902 Hassani, B., and Atkinson, G. M., 2016. Site effects model for Central and Eastern
903 North America based on peak frequency, *Bull. Seismol. Soc. Am*, **106**, 2197-
904 2213. doi.org/10.1785/0120160049.

905 Hu, Y.H., Hwang, J.N., 2002. Handbook of neural network signal processing. *Acoust*
906 *Soc Am*, **111**,2525–2526. doi.org/10.1121/1.1480419.

907 Idriss, I. M., 2011. Use of V_{s30} to represent local site conditions, In Proceedings of the
908 4th IASPEI/IAEE international symposium. Effects of source geology on seismic
909 motion, August (p. 23-26).

910 Kamai, R., Abrahamson, N. A., and Silva,W. J., 2014. Nonlinear horizontal site
911 amplification for constraining the NGA-West2 GMPEs, *Earthquake Spectra*, **30**
912 ,1223– 1240. doi.org/10.1193/070113EQS187M.

913 Konno, K., Ohmachi, T., 1998. Ground-motion Characteristics Estimated from
914 Spectral Ratio between Horizontal and Vertical Components of Microtremor,
915 *Bulletin seism. Soc. Am* **88**, 228-241.

916 Kwok, A. O., Stewart, J. P., and Hashash, Y. M., 2008. Nonlinear ground response
917 analysis of Turkey Flat shallow stiff-soil site to strong ground motion, *Bull.*
918 *Seismol. Soc. Am* **98**, 331–343. doi.org/10.1785/0120070009.

919 Laurendeau, A., Bard, P. Y., Hollender, F., Perron, V., Foundotos, L., Ktenidou, O. J.,
920 and Hernandez, B., 2018. Derivation of consistent hard rock ($1000 < V_s < 3000$
921 m/s) GMPEs from surface and down-hole recordings: analysis of KiK-net
922 data. *Bull. Earthq. Eng*, **16**, 2253-2284. doi.org/10.1007/s10518-017-0142-6.

923 Maufroy, E., Chaljub, E., Theodoulidis, N.P., Roumelioti, Z., Hollender, F., Bard, P.-Y.
924 de Martin, F., Guyonnet-Benaize, C. and Margerin, L., 2017.Source-Related
925 Variability of Site Response in the Mygdonian Basin (Greece) from

926 Accelerometric Recordings and 3D Numerical Simulations, *Bull. Seismol. Soc.*
927 *Am* **107**,787–808. doi.org/10.1785/0120160107.

928 Peter, A., Harald, B., Wolfgang, M., 2008. A learning rule for very simple universal
929 approximators consisting of a single layer of perceptrons, *Neural Netw* **21**,786–
930 795. DOI: 10.1016/j.neunet.2007.12.036.

931 Régnier, J., Cadet, H., Bonilla, L, Bertand, E., and Semblat, J. F., 2013. Assessing
932 Nonlinear Behavior of Soils in Seismic Site Response: Statistical Analysis on
933 KiK-net Strong-Motion Data, *Bull. Seismol. Soc. Am*, **103**, 1750-1770. doi:
934 10.1785/0120120240.

935 Régnier, J., Cadet, H., Bonilla, L. F., Bertrand, E., & Semblat, J. F. (2013). Assessing
936 nonlinear behavior of soils in seismic site response: Statistical analysis on KiK-
937 net strong-motion data. *Bulletin of the Seismological Society of America*, *103*(3),
938 1750-1770.

939 Régnier, J., Bonilla, L. F., Bertrand, E., and Semblat, J.-F., 2014. Influence of the V_s
940 Profiles beyond 30 m Depth on Linear Site Effects: Assessment from the KiK-
941 net Data, *Bull. Seismol. Soc. Am*, **104**, 2337-2348.
942 doi.org/10.1785/0120140018.

943 Régnier, J., Cadet, H., and Bard, P.-Y., 2016a. Empirical Quantification of the Impact
944 of Nonlinear Soil Behavior on Site Response, *Bull. Seismol. Soc. Am*, **106**,
945 1710-1719. doi.org/10.1785/0120150199

946 Régnier, J., Bonilla, L.-F., Bard, P.-Y., Bertrand, E., Hollender, F., Kawase, H., Sicilia,
947 D., Arduino, P., Amorosi, A., Asimaki, D., Boldini, D., Chen, L., Chiaradonna, A.,
948 DeMartin, F., Ebrille, M., Elgamal, A., Falcone, G., Foerster, E., Foti, S., Garini,
949 E., Gazetas, G., Gélis, C., Ghofrani, A., Giannakou, A., Gingery, J.R., Glinsky,

950 N., Harmon, J., Hashash, Y., Iai, S., Jeremić, B., Kramer, S., Kontoe, S.,
951 Kristek, J., Lanzo, G., di Lernia, A., Lopez-Caballero, F., Marot, M., McAllister,
952 G., Mercerat, E. D., Moczo, P., Montoya-Noguera, S., Musgrove, M., Nieto-
953 Ferro, A., Pagliaroli, A., Pisanò, F., Richterova, A., Sajana, S., Santisi d'Avila,
954 M.P., Shi, J., Silvestri F., Taiebat, M., Tropeano, G., Verrucci L., and Watanabe
955 K., 2016b. International benchmark on numerical simulations for 1D, non-linear
956 site response (PRENOLIN): verification phase based on canonical cases. *Bull.*
957 *seism. Soc. Am*, **106**, 2112–2135. doi: 10.1785/0120150284.

958 Régnier, J., Bonilla, L.-F., Bard, P.-Y., Bertrand, E., Hollender, F., Kawase, H., Sicilia,
959 D., Arduino, P., Amorosi, A., Asimaki, D., Boldini, D., Chen, L., Chiaradonna,
960 A., DeMartin, F., Elgamal, A., Falcone, G., Foerster, E., Foti, S., Garini, E.,
961 Gazetas, G., Gélis, C., Ghofrani, A., Giannakou, A., Gingery, J., Glinesky, N.,
962 Harmon, J., Hashash, Y., Iai, S., Kramer, S., Kontoe, S., Kristek, J., Lanzo, G.,
963 di Lernia, A., Lopez-Caballero, F., Marot, M., McAllister, G., Mercerat, E. D.,
964 Moczo, P., Montoya-Noguera, S., Musgrove, M., Nieto-Ferro, A., Pagliaroli, A.,
965 Passeri, F., Richterova, A., Sajana, S., Santisi d'Avila, M. P., Shi, J., Silvestri,
966 F., Taiebat, M., Tropeano, G., Vandeputte, D., and Verrucci, L., 2018.
967 PRENOLIN: International Benchmark on 1D Nonlinear Site-Response
968 Analysis—Validation Phase Exercise, *Bull. seism. Soc. Am*, **108**, 876–900.
969 doi: 10.1785/0120170210.

970 Robitaille, B., Marcos, B., Veillette, M., and Payr, G., 1996. Modified quasi-Newton
971 methods for training neural networks, *Comput Chem Eng*, **20**, 1133–1140.
972 doi.org/10.1016/0098-1354(95)00228-6.

973 Sandikkaya, M. A., S. Akkar, and bard, P-Y., 2013. A Nonlinear Site-Amplification
974 Model for the Next Pan-European Ground-Motion Prediction Equations, *Bull.*
975 *seism. Soc. Am*, **103**,19-32. doi.org/10.1785/0120120008.

976 Seyhan, E., and Stewart, J. P., 2014. Semi-empirical nonlinear site amplification from
977 NGAWest2 data and simulations, *Earthquake Spectra*, **30**, 1241– 1256.
978 doi.org/10.1193/063013EQS181M.

979 Stewart, J. P., 2008. Benchmarking of nonlinear geotechnical ground response
980 analysis procedures, PEER Report 2008/04, Pacific Earthquake Engineering
981 Research Center, University of California, Berkeley, California, 186 pp.

982 Stewart, J. P., and A. O. L. Kwok., 2008. Nonlinear seismic ground response
983 analysis: Code usage protocols and verification against vertical array data,
984 *Geotechnical Earthquake Engineering and Soil Dynamics IV, geotechnical*
985 *Special Publication*, **181**, 1-24. escholarship.org/uc/item/7db3d49z.

986 Stewart, J. P., and Kwok, A. O., 2009. Nonlinear seismic ground response analysis:
987 Protocols and verification against array data, 2009 PEER Annu. Meet., San
988 Francisco, California, 84 pp.

989 Trifunac, M. D.,and Brady, A. G., 1975. A study on the duration of strong earthquake
990 ground motion, *Bull. Seism. Soc. Amer.* **65**, 581-626.

991 Walling, M., Silva, W., and Abrahamson, N., 2008. Nonlinear site amplification factors
992 for constraining the NGA models, *Earthq. Spectra*, **24**, 243–255.
993 doi.org/10.1193/1.2934350.

994 Wierenga, B., and Kluytmans, J., 1994. Neural nets versus marketing models in time
995 series analysis: a simulation studies. Proceedings of the 23-annual conference
996 of the European Marketing Association, Maastricht, 1139–1153.

997 Wolfgang, M., 1997. Networks of spiking neurons: the third generation of neural
998 network models. *Neural Netw* **10**,1659–1671. doi.org/10.1016/S0893-
999 6080(97)00011-7.

Figures Captions

Figure 1 Road-map to obtain non-linear to linear site response ratio (RSR_{NL-GM}). In step 1 the initial dataset of RSR_{NL} , SCPs and GMIM are presented (Régnier et al., 2016). Step 2: the RSR_{NL} are normalized by f_{NL} . Step 3: Seven different "advanced data sets" (RSR_{NL-GM}) are produced. Step 4 illustrates the sensitivity study to choose the best SCPs and GMIMs in the normalized frequency domain. Step 5: the best model of RSR_{NL-GM} in the absolute frequency domain is established using ANN approach.

Figure 2 Statistical distribution of data and variation of RSR_{NL-GM} with shaking intensity on the example of the PGA GMIM. The three top subplots (A1, A2 and A3) display the CDF of PGA, the number of sites available per fractile of PGA and their distribution as a function of f/f_{NL} , respectively. The colored circles and lines represent the 15 PGA-bins. The two bottom plots show the average and "standard deviation" of $RSR_{NL-GM}(f/f_{NL})$ for each PGA-bin, respectively. The 15 PGA-bins (circles and lines colors) correspond to regularly spaced fractiles of the PGA CDF, every 10%, from F10 to F50, and every 5% from F55 to F100.

Figure 3 Empirical cumulative distribution function (CDF) of the original set of 2927 KiK-net recordings according to each considered GMIM: PGA (top left), PGV (top right), CAV (second row from top, left), I_A (right), D_T (third row from top, left), A_{rms} (right) and PGV/V_{s30} (bottom).

Figure 4 Empirical cumulative distribution function (CDF) of the original set of 2927 KiK-net recordings according to each considered site proxy: V_{s30} (top left), V_{smin} (top right), B_{30} (middle left), f_{0HV} (middle right), A_{0HV} (bottom left). The bottom right plot displays the CDF of the measured f_{NL} values for the considered KiK-net data set.

Figure 5 Scatter plots displaying the correlation (or absence of correlation) between all the considered GMIMs. The value given at the top of each plot represents the correlation coefficient between the corresponding pair of GMIMs.

Figure 6 Scatter plots displaying the correlation (or absence of correlation) between the different site-condition proxies (SCPs). The value given at the top of each plot represents the correlation coefficient between the corresponding pair of SCPs.

Figure 7 Initial variability of the seven advanced data sets (corresponding to the seven considered GMIMs) as a function of normalized frequency f/f_{NL} (left), and absolute frequency f (right). This variability is quantified by the $\sigma_{ref}(RSR_{NL-GM})$ as defined in [equation 7] in \log_{10} values.

Figure 8 General pattern of the ANN models consider here: The left part corresponds to the input layer (one GMIM, plus one or more SCPs), the right part corresponds to the outputs to be predicted by the ANN (RSR_{NL-GM} , in either absolute or normalized frequency), and the central part the combinations performed with the intermediate hidden layer. W and b are the synaptic weights and bias between two neurons, respectively. The shape of function in the box represents the optimal activation functions finally selected: non-linear (tanh) for the hidden layer, and linear for the output layer.

Figure 9 Performance of various GMIMs and SCPs in reducing the initial RSR_{NL-GM} variability, as a function of f/f_{NL} . The top-left frame display the variance reduction coefficient (R_c) for all the one-GMIM ANN models. The other frames represent in a similar way the performance of all (one-GMIM, one-SCP) ANN models: each frame correspond to one specific SCP (V_{s30} , V_{smin} , B_{30} , f_{0HV} , A_{0HV}), and the 7 different GMIMs (PGA, PGV, CAV, I_A , DT, A_{rms} , PGV/V_{s30}), with the same labeling as in the top left frame.

Figure 10 Sensitivity of the mean variance reduction " $\mu(R_c)$ " (arithmetic average over the normalized frequency range [0.25-0.4], in %) to the ANN model. The horizontal length of each colored bar display the $\mu(R_c)$ values listed in Table 1: the color code correspond to the 7 considered GMIMs, and the vertical axis to the various site proxies considered as input.

Figure 11 Variance reduction coefficient (R_c) for the seven $RSR_{NL-GM}(f/f_{NL})$ models considering V_{s30} and f_{0HV} as input SCPs. [PGV/V_{s30} , V_{s30} , f_{0HV}] is considered as the optimal

combination providing the best RSR_{NL-GM} predictions. The grey dashed vertical lines indicate the f/f_{NL} band [0.25, 4.0] over which the mean $\mu(R_c)$ values are computed.

Figure 12 Dependence of residuals from RSR_{NL-GM} final absolute frequency model according to V_{s30} , f_{0HV} and PGV/V_{s30} , respectively. The three left plots correspond to frequency = 2.4 Hz and the right plots are for a frequency = 8 Hz. We illustrate the Mean residuals and standard deviations in the different metadata ranges. The circles show average residuals in bins; the vertical bars correspond to the variability (two standard deviations) within each bin, while the horizontal bars represent the standard deviation of the residuals for the whole model.

Figure 13 Variation of median $RSR_{NL-GM}(f)$ predicted for increasing values of PGV/V_{s30} (corresponding to the mean bin values, in %). Several pairs of (V_{s30}, f_{0HV}) are considered: their choice is based primarily on their location within the validity domain of the model (as indicated in the frame inserted in (A): red circles) and on the wish to explore a wide range of sites: soft to stiff, shallow to deep sites, as indicated by their V_{s30} values (160, 300, 800 m/s) and f_{0HV} values (0.3, 1, 3, 9 Hz).

Figure 14 Variation of median RSR_{NL-GM} predicted for different values of V_{s30} (300, 400, 600, 800 m/s, left), and for several values of f_{0HV} (0.3, 1.0, 3.0, 9.0 Hz, right). The PGV/V_{s30} value (0.02 %) has been considered in order to be well beyond the onset of non-linear behavior. In the case where V_{s30} is varying we take $f_{0HV} = 3.0$ Hz (left). In the case where taken f_{0HV} as variable we fix V_{s30} at a 300 m/s value.

Figures

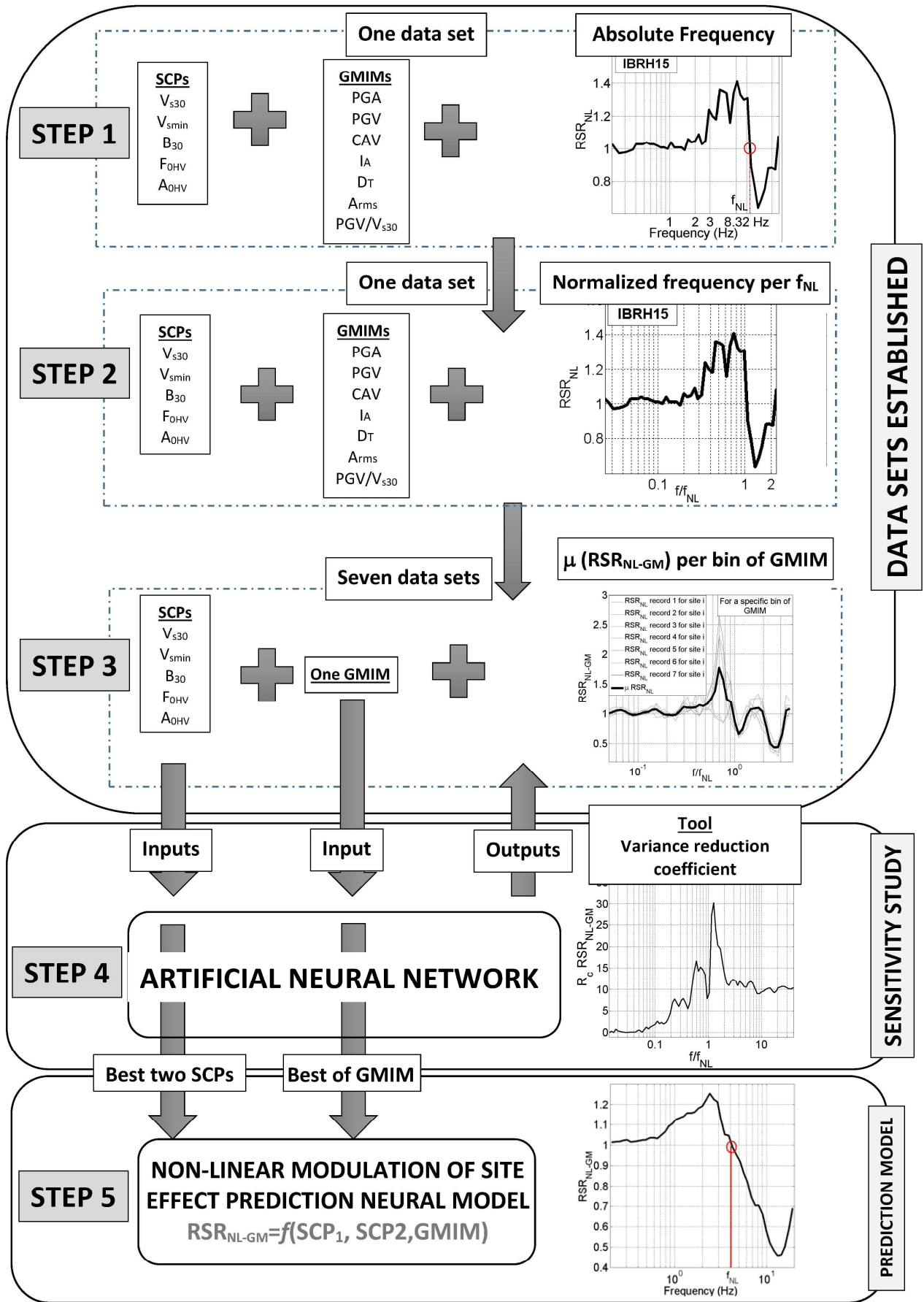


Figure 1

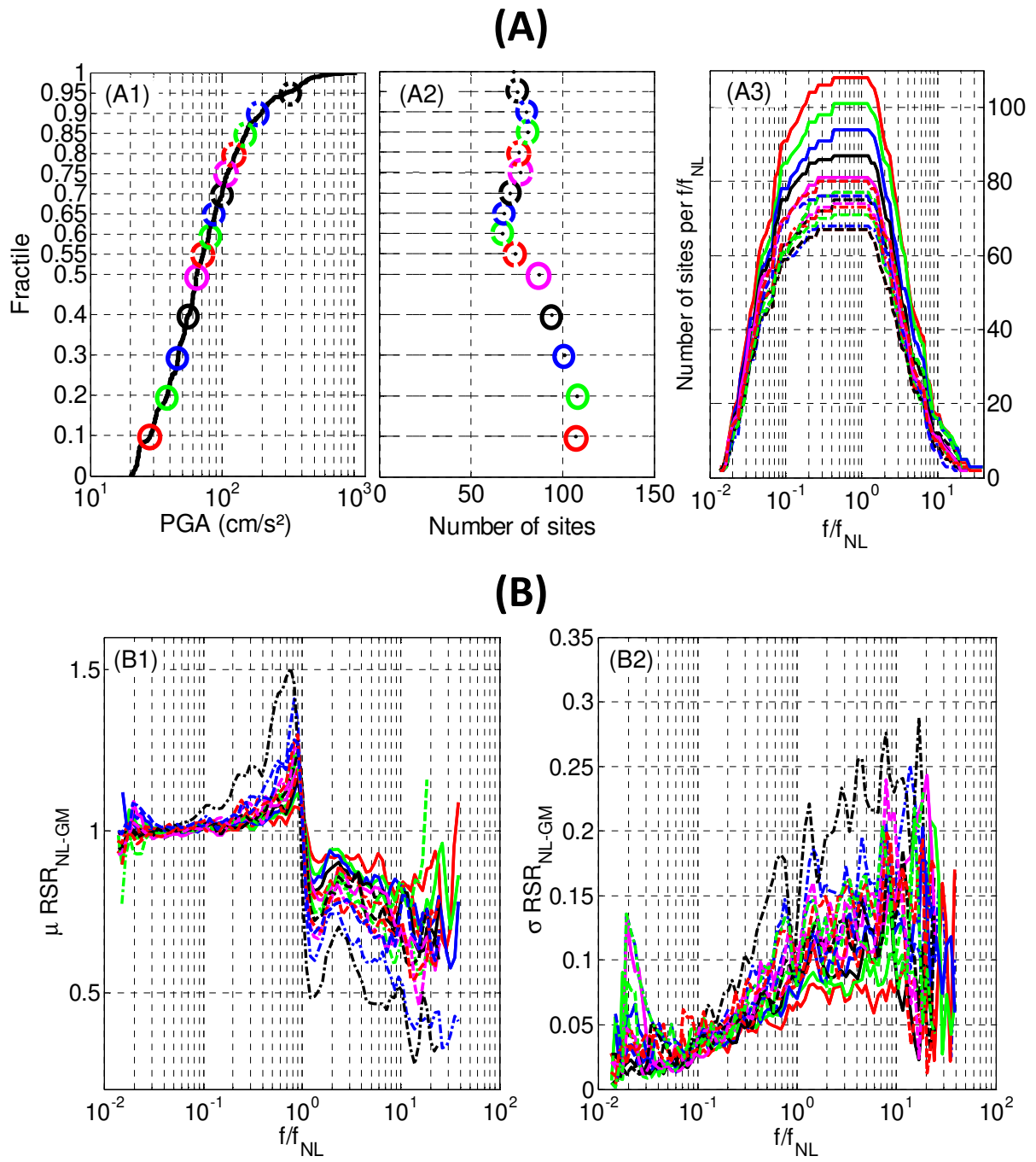


Figure 2

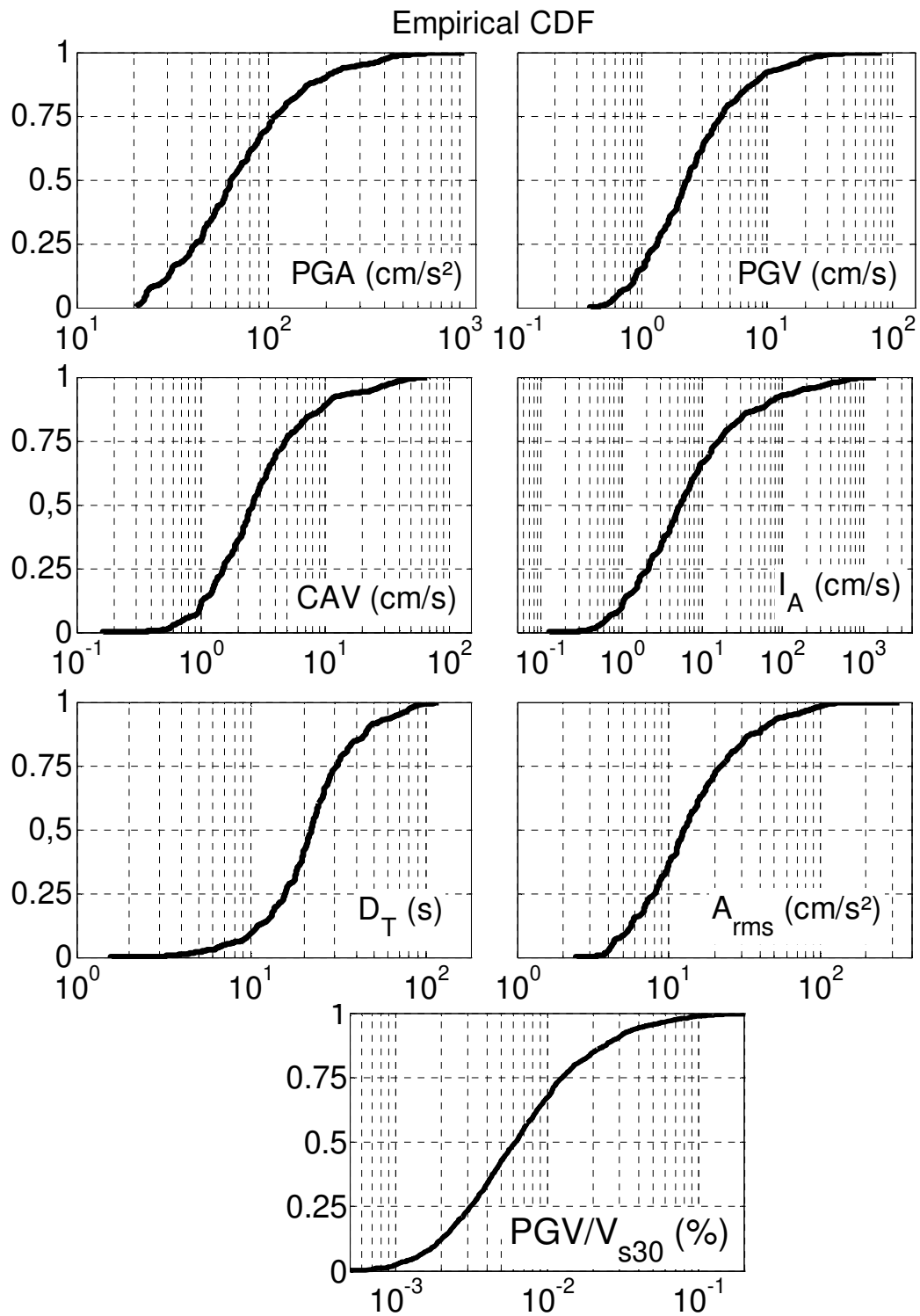


Figure 3

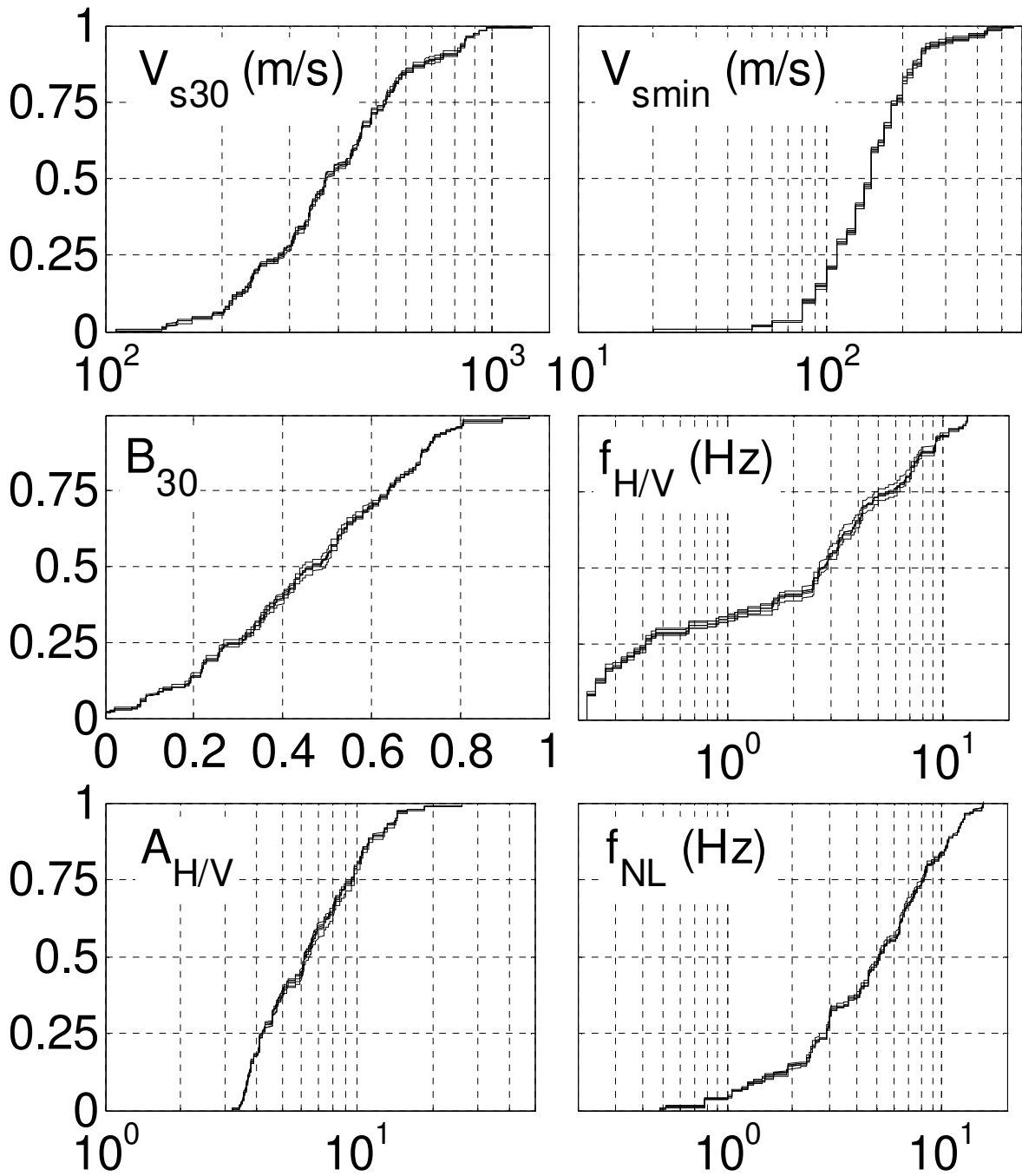


Figure 4

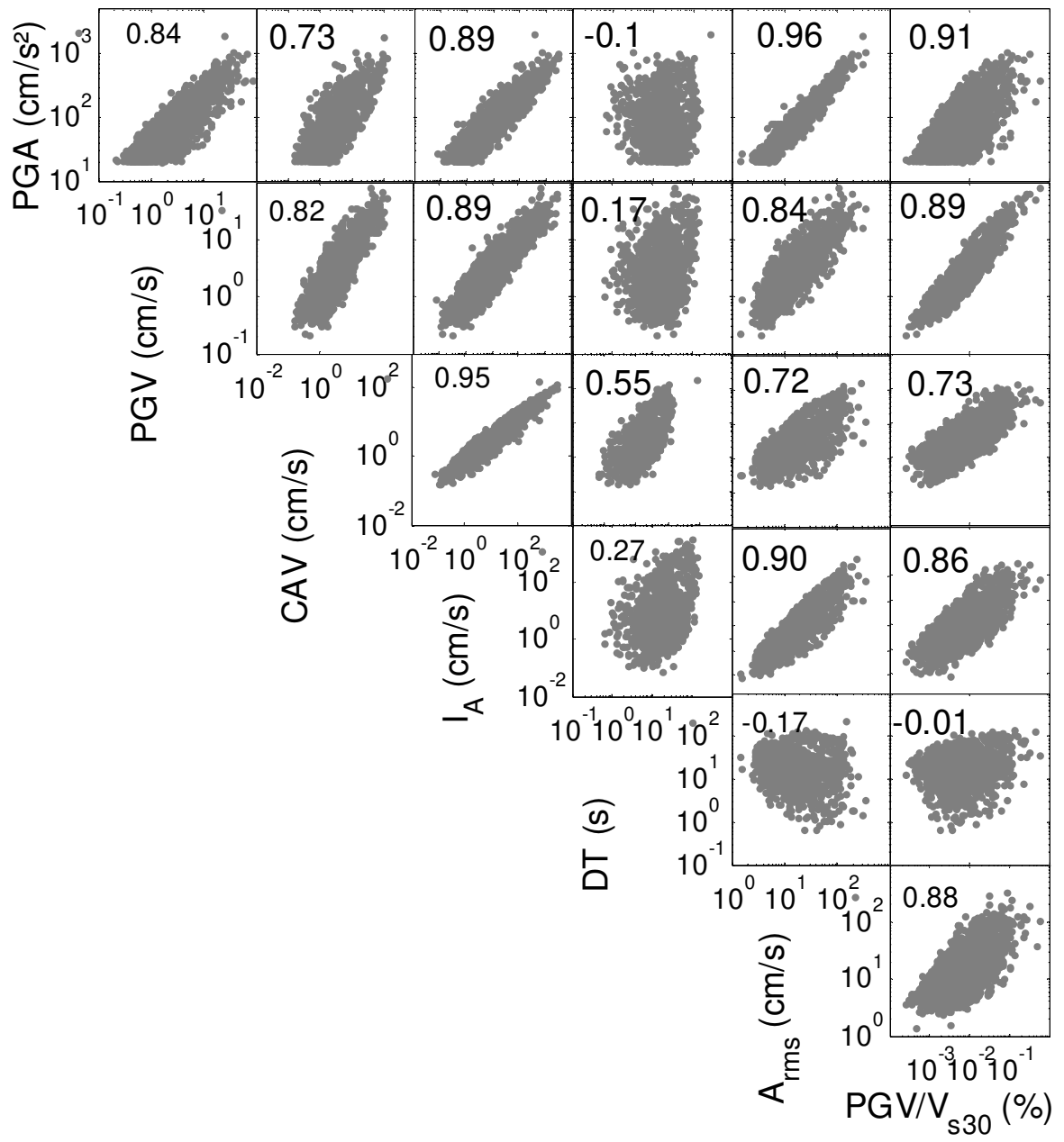


Figure 5

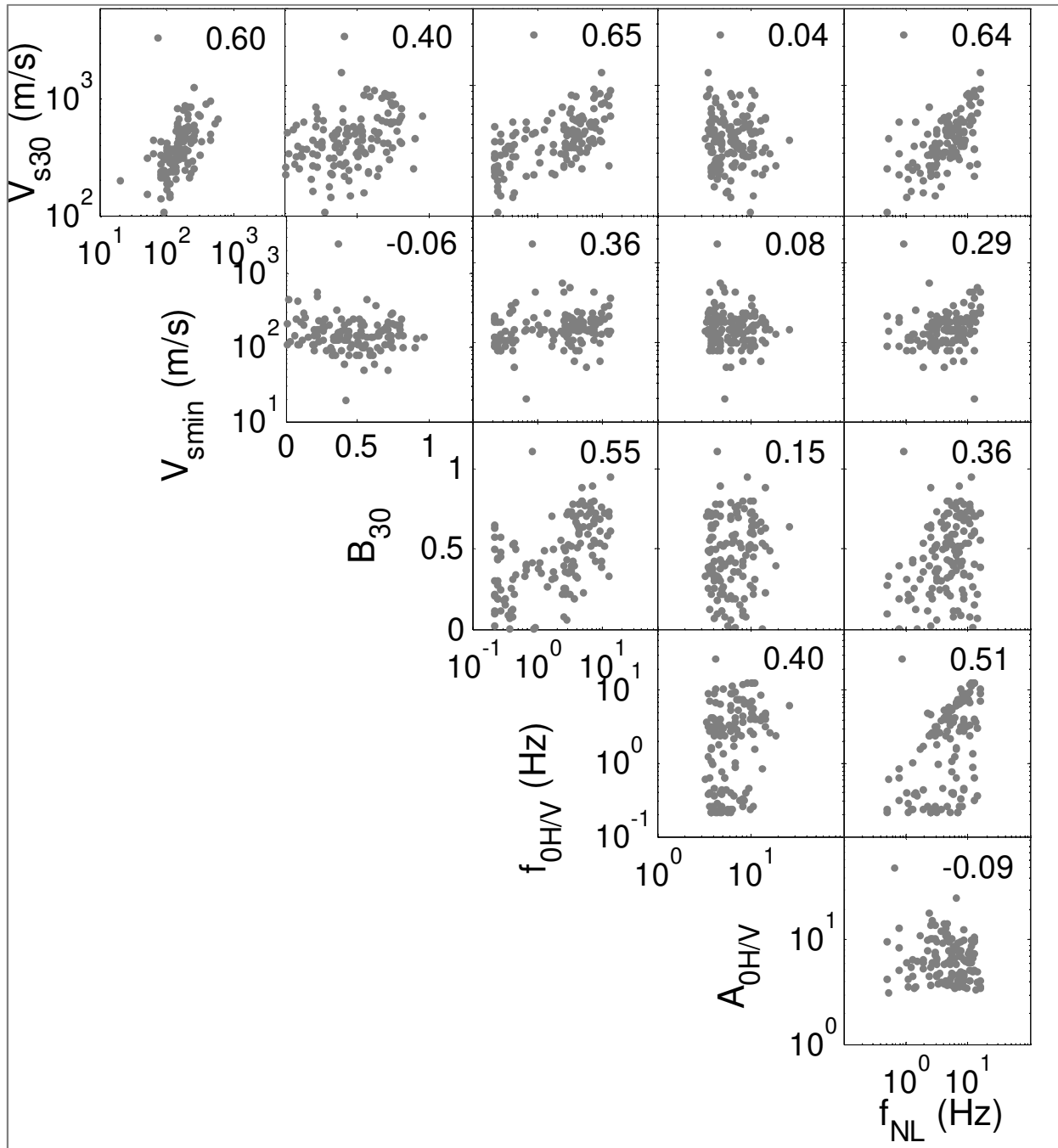


Figure 6

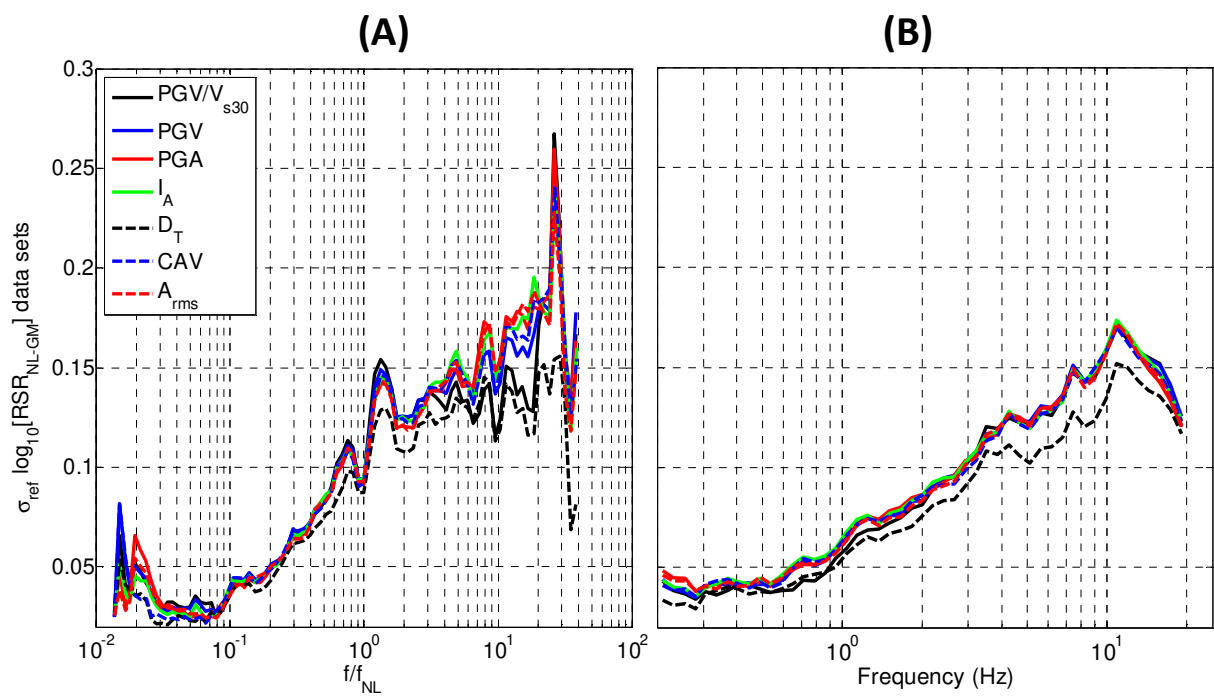


Figure 7

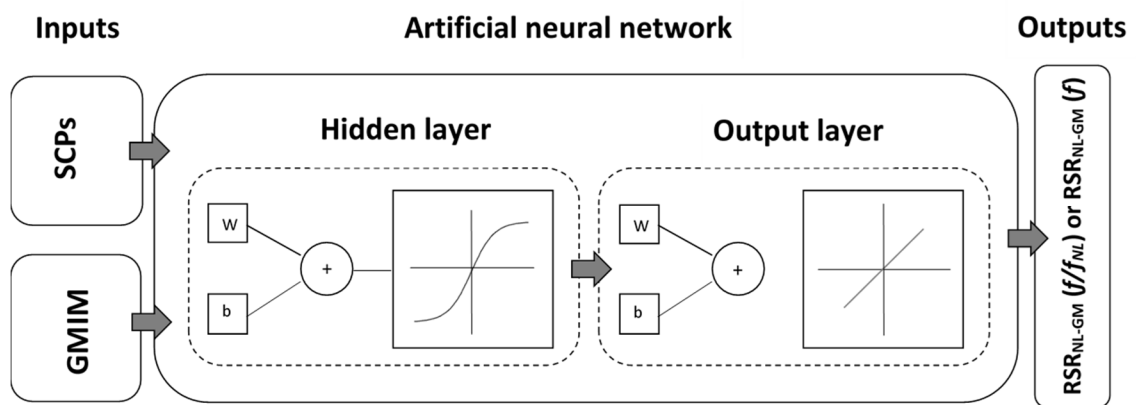


Figure 8

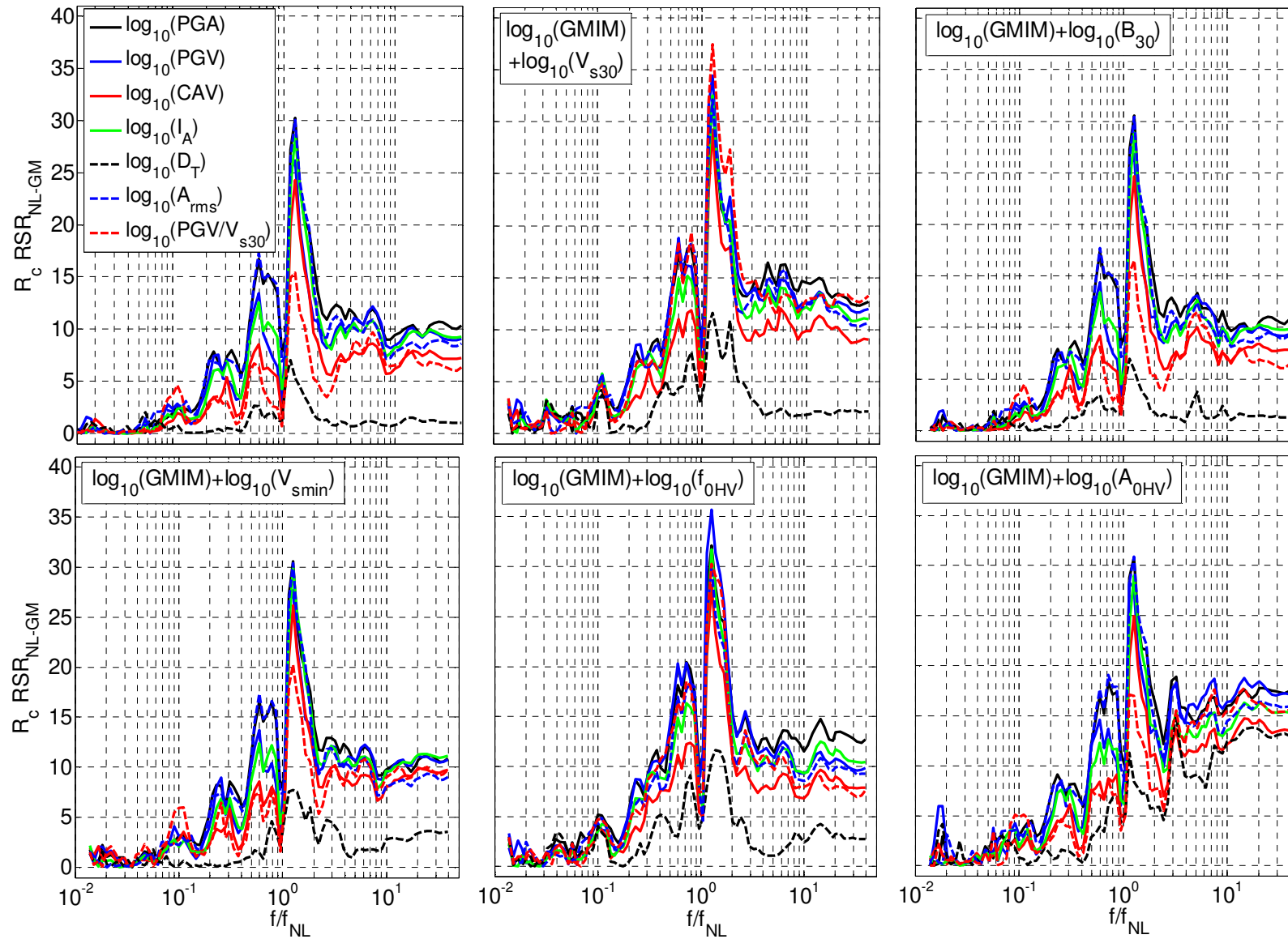


Figure 9

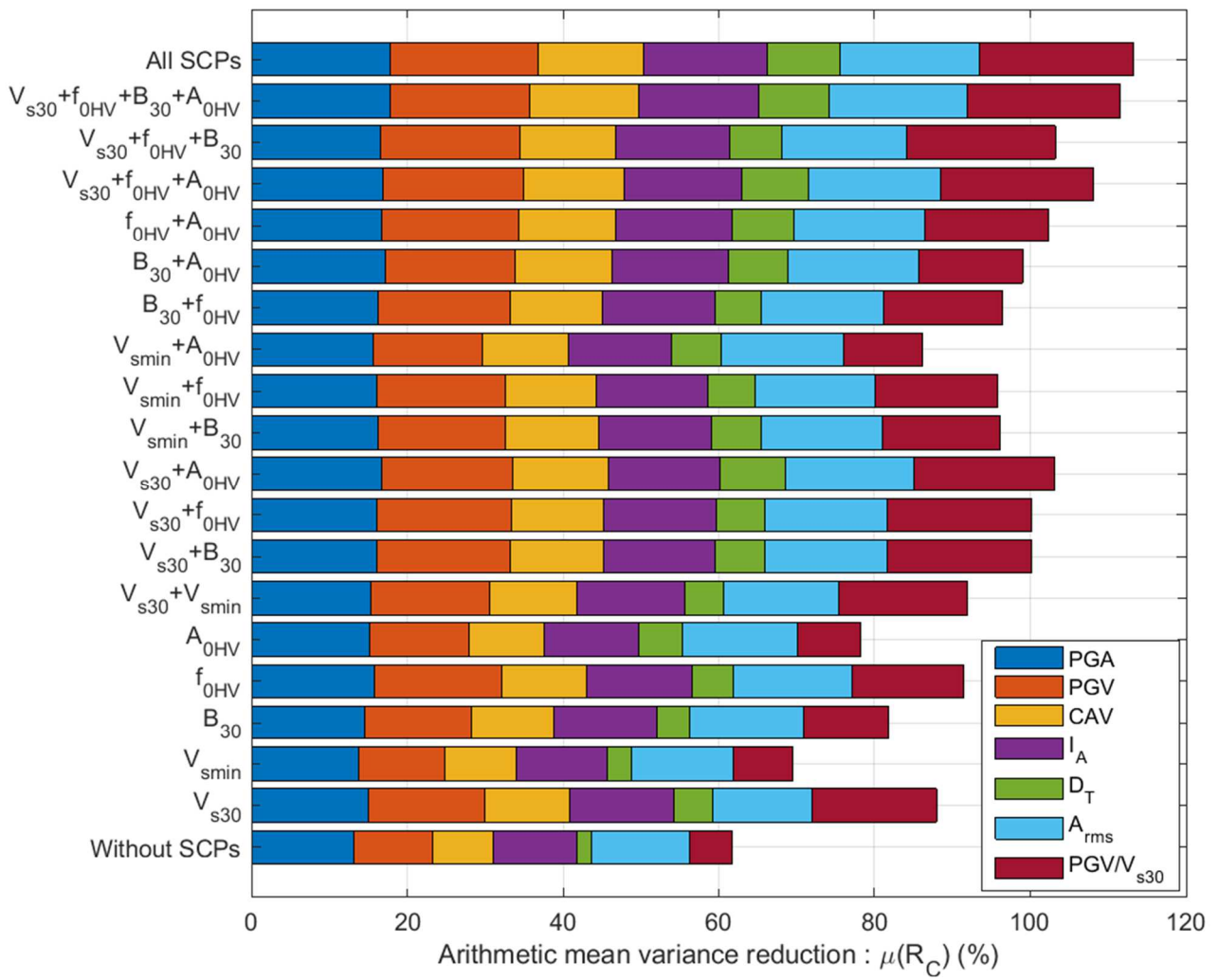


Figure 10

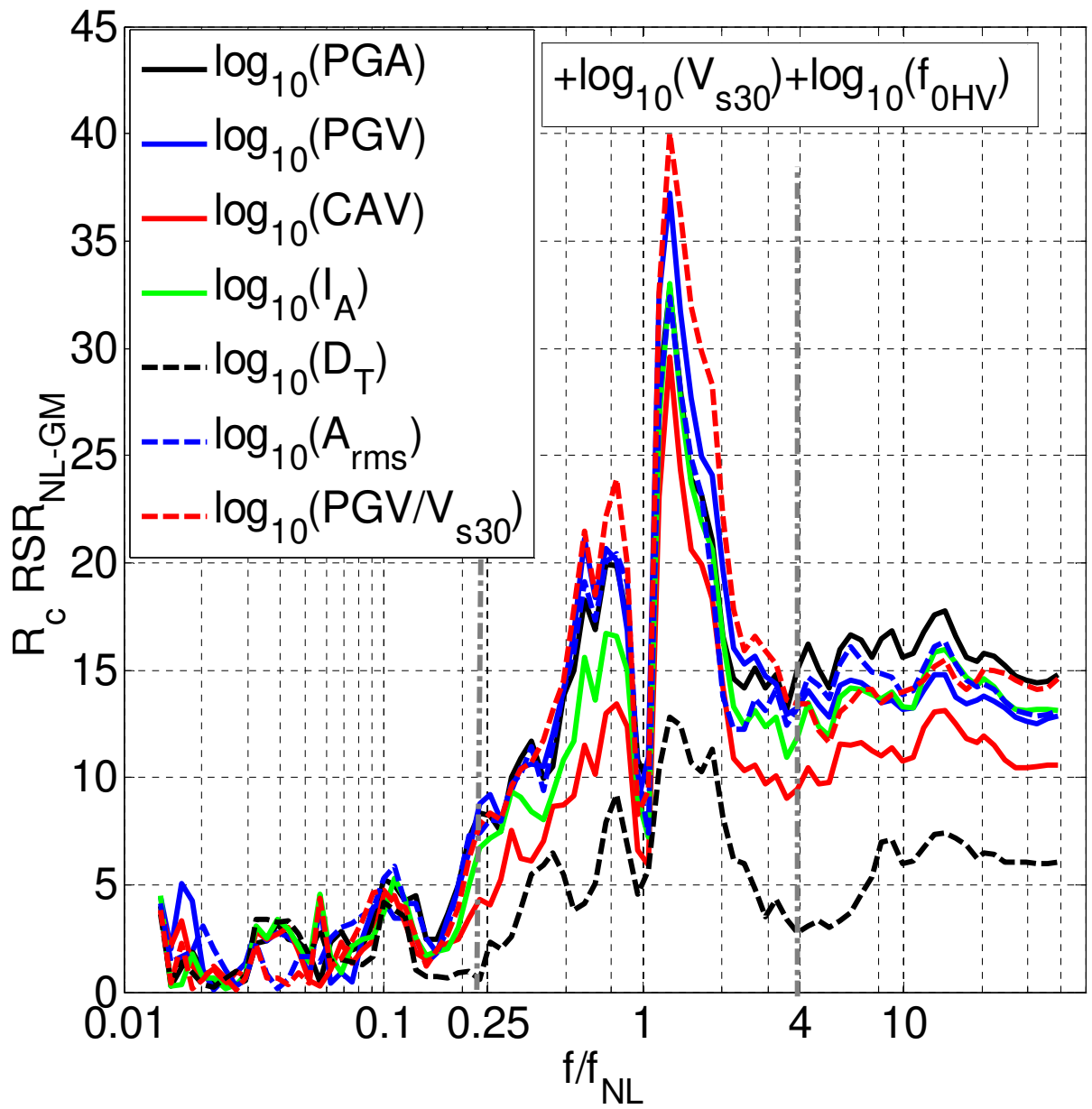


Figure 11

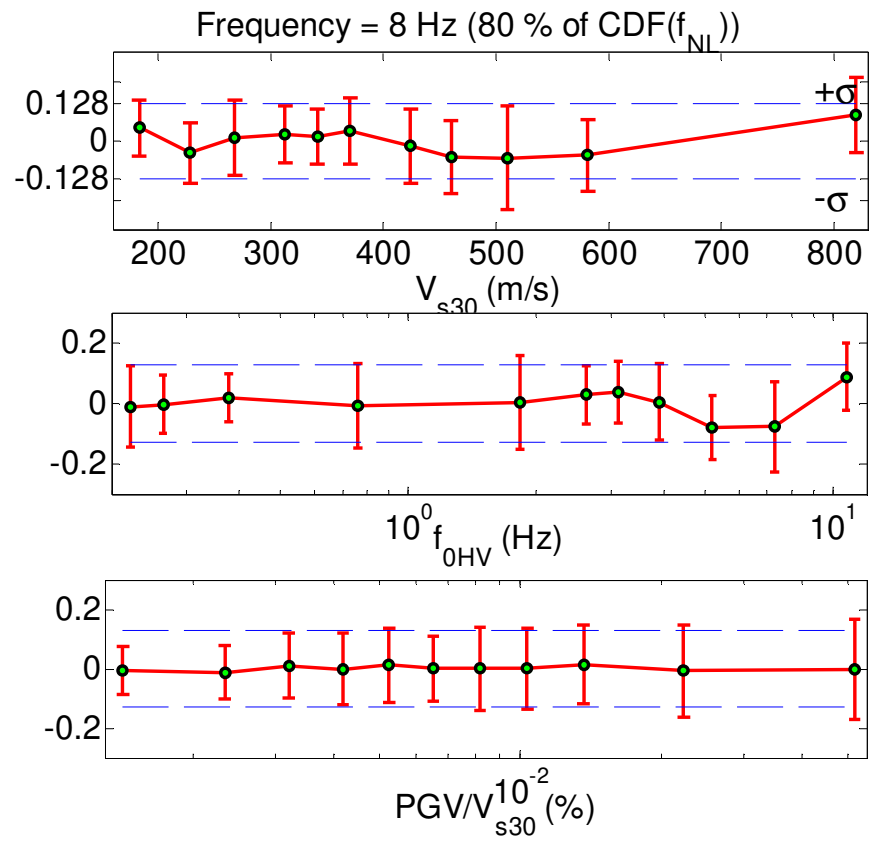
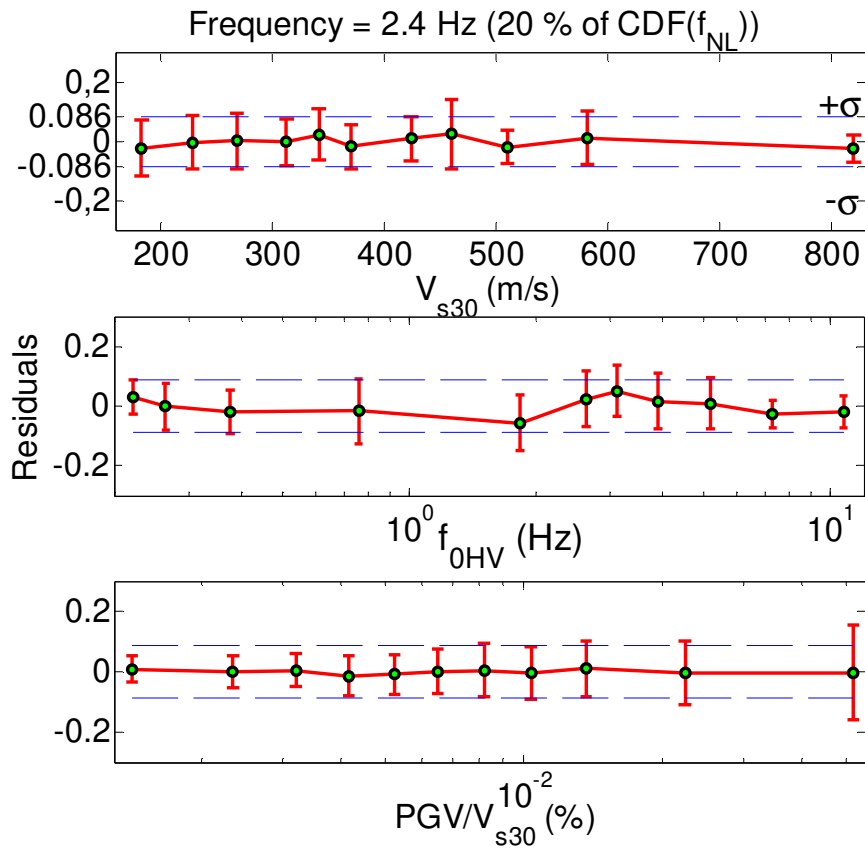


Figure 12

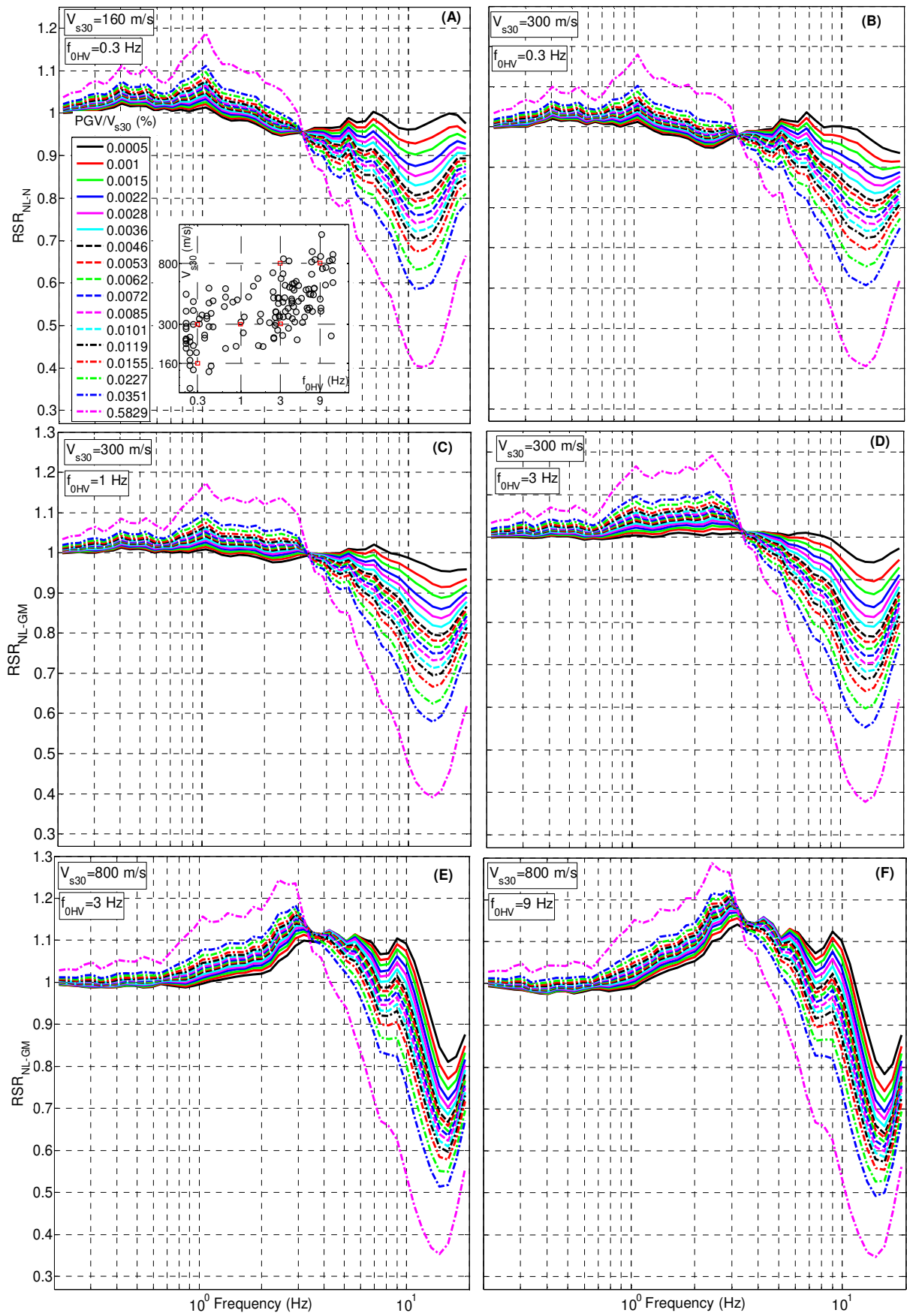


Figure 13

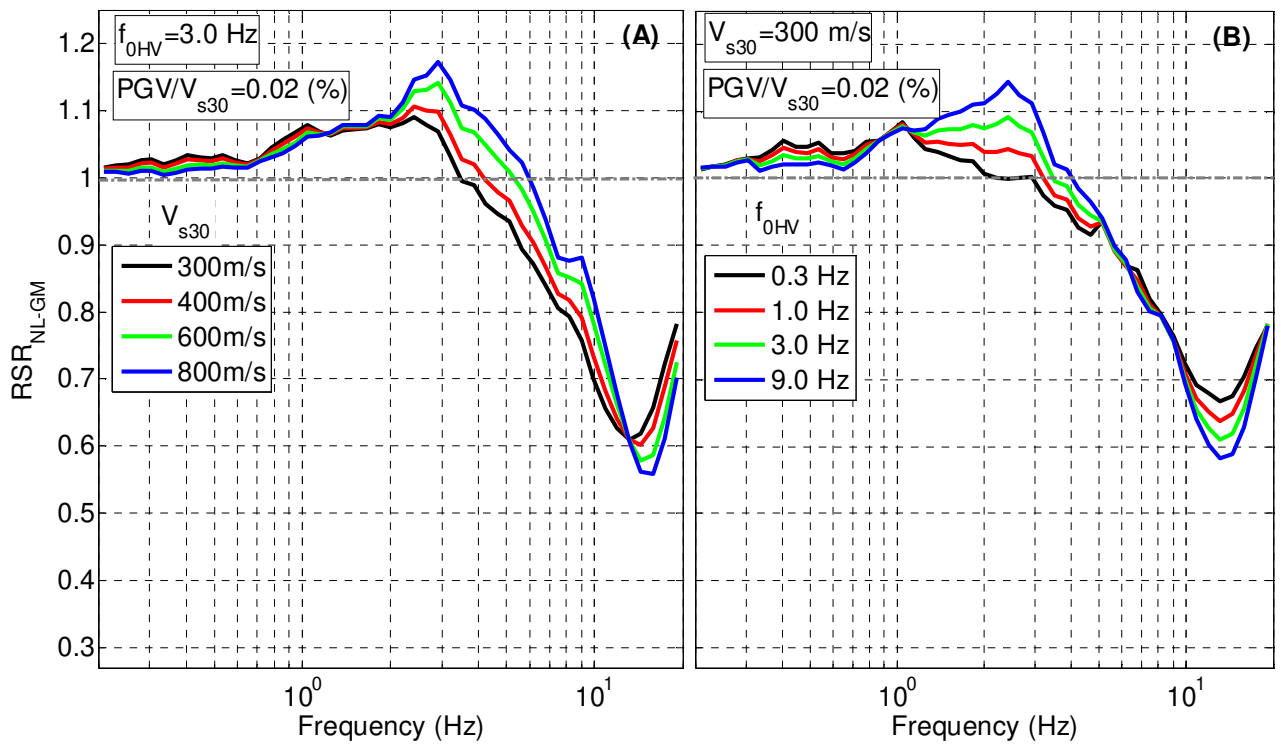
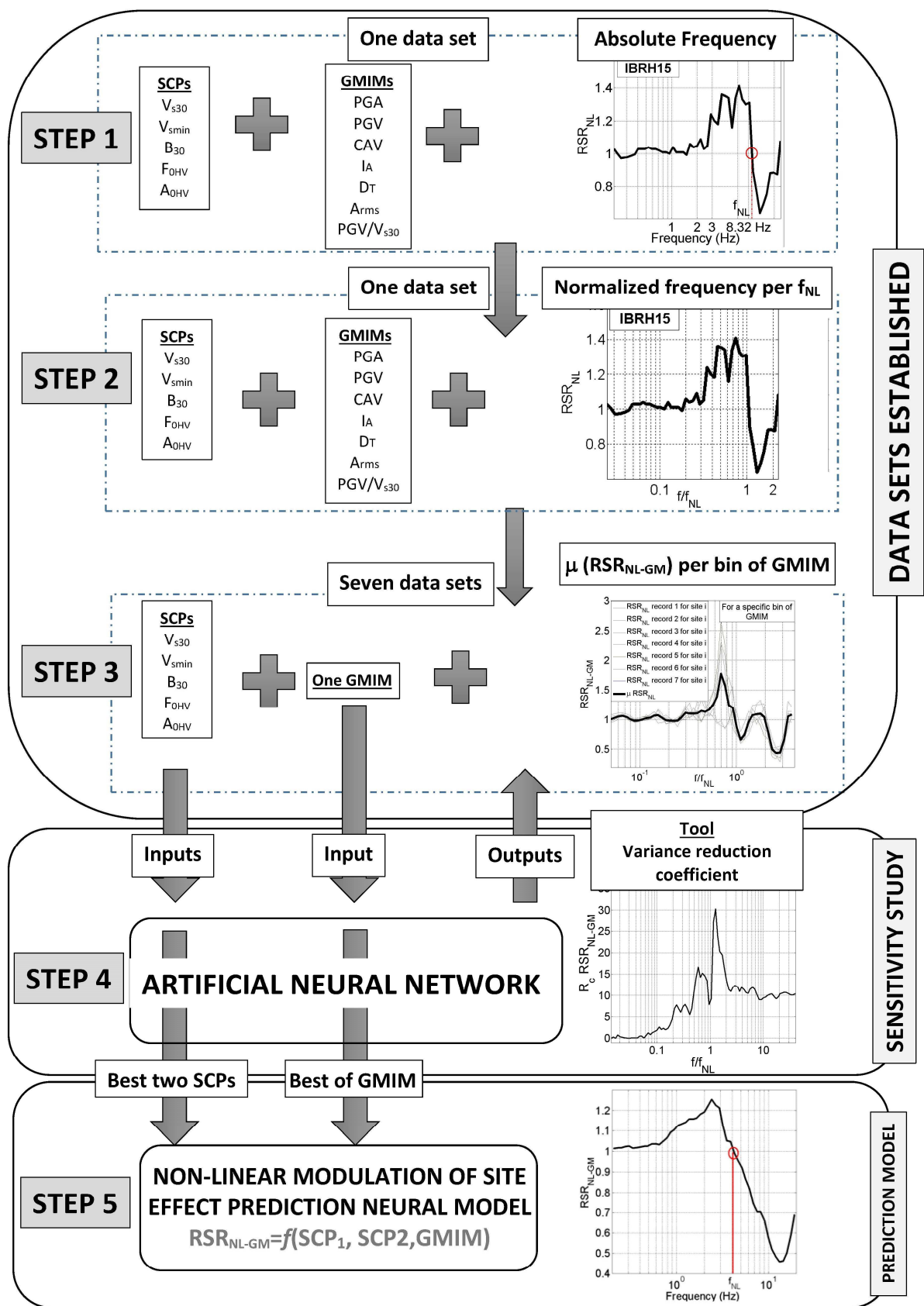


Figure 14

Table

Table 1 : Mean variance reduction ($\mu(R_c)$, arithmetic average of $R_c(f/f_{NL})$ over the $[0.25, 4]$ f/f_{NL} interval, in %) for the 140 considered ANN models. One GMIM and two/three/four/all SCP are chosen as input to build the 140 ANN-RSR models.

$\mu(R_c)$ in %	PGA	PGV	CAV	I _A	D _T	A _{rms}	PGV/V _{S30}
Without SCPs	13.21	10.05	7.80	10.73	1.86	12.65	5.39
V _{S30}	14.96	15.02	10.87	13.38	5.02	12.77	15.92
V _{smin}	13.7	11.2	9.1	11.64	3.16	13.1	7.67
B ₃₀	14.61	13.65	10.57	13.25	4.18	14.69	10.78
F _{0HV}	15.73	16.43	10.89	13.53	5.23	15.29	14.35
A _{0HV}	15.24	12.77	9.54	12.1	5.61	14.88	8.06
V _{S30} +V _{smin}	15.34	15.29	11.22	13.72	5.06	14.84	16.46
V _{S30} +B ₃₀	16.15	17.01	11.99	14.44	6.30	15.79	18.47
V _{S30} +f _{0HV}	16.16	17.26	11.86	14.34	6.27	15.72	18.59
V _{S30} +A _{0HV}	16.68	16.91	12.31	14.30	8.30	16.53	18.16
V _{smin} +B ₃₀	16.28	16.29	12.08	14.44	6.31	15.65	15.07
V _{smin} +f _{0HV}	16.10	16.56	11.67	14.20	6.16	15.44	15.67
V _{smin} +A _{0HV}	15.60	14.05	11.03	13.20	6.41	15.67	10.25
B ₃₀ +f _{0HV}	16.21	17.00	11.89	14.42	5.97	15.66	15.32
B ₃₀ +A _{0HV}	17.19	16.73	12.38	14.95	7.64	16.84	13.32
F _{0HV} +A _{0HV}	16.79	17.50	12.47	15.02	7.86	16.80	15.93
V _{S30} +f _{0HV} +A _{0HV}	16.86	18.03	12.96	15.09	8.56	17.00	19.56
V _{S30} +f _{0HV} +B ₃₀	16.62	17.79	12.36	14.64	6.65	16.13	19.02
V _{S30} +f _{0HV} +B ₃₀ +A _{0HV}	17.82	17.93	14.05	15.35	9.04	17.67	19.66
All SCPs	17.80	18.99	13.55	15.96	9.30	17.82	19.76



Road-map to obtain non-linear to linear site response ratio (RSR_{NL-GM}). In step 1 the initial dataset of RSR_{NL} , SCPs and GMIM are presented (Régnier et al., 2016). Step 2: the RSR_{NL} are normalized by f_{NL} . Step 3: Seven different "advanced data sets" (RSR_{NL-GM}) are produced. Step 4 illustrates the sensitivity study to choose the best SCPs and GMIMs in the normalized frequency domain. Step 5: the best model of RSR_{NL-GM} in the absolute frequency domain is established using ANN approach.